A multifaceted isoneutral eddy transport diagnostic framework and its application in the Southern Ocean

Jingwei Xie[1,2], Hailong Liu[1,2,3*], and Pengfei Lin[1,2]

[1]LASG, Institute of Atmospheric Physics, Chinese Academy of Sciences, Beijing 100029, China
[2]College of Earth and Planetary Sciences, University of Chinese Academy of Sciences, Beijing 100049, China
[3]Center for Ocean Mega-Science, Chinese Academy of Sciences, Qingdao 266071, China

Key Points:

- The Southern Ocean transport processes have intense anisotropy
- The stationary and topographic effect is crucial for the subfilter transport
- The complete subgrid flux should be considered for the mesoscale eddy scheme

* Corresponding author: Hailong Liu, lhl@lasg.iap.ac.cn

Abstract

We propose a multifaceted isoneutral eddy transport diagnostic framework that combines the stationary-transient and Leonard's decomposition in large eddy simulation (LES). We diagnose the subfilter flux, the isotropic transport coefficient, and the anisotropic transport tensor or eigenvalues in the Southern Ocean (SO). The anisotropic tensor greatly reduces the reconstruction error of the subfilter flux because of its ability to distinguish the directionality of dynamic information, especially the topographic effect. A thorough analysis of the anisotropic tensor or transport eigenvalues reveals that the sign combination of the transport eigenvalues of the symmetric tensor links to the evolution of domain-integral large-scale PV enstrophy and the combination of different signs is most often, meaning the dominance of filamentation process in the SO. In the region with intense anisotropy, the dominant eigenvector tends to be perpendicular to the large-scale PV gradient, indicating an important role of the PV barrier mechanism in the SO transport process. The two distinct decompositions leveraged in our framework generate intriguing and profound results. Under the stationary-transient decomposition, we find a significant stationary contribution and the duality of the topographic effect which can not only anchors stationary structures but also organizes transient motions. Leonard's decomposition, allows us to investigate the collective effects of the standing wave train, cross-scale interaction, and subfilter eddy-eddy interaction on the filtered space-time scale. We emphasize the complete subgrid flux, not the mere Reynolds term, and the LES framework needs to be considered in the subgrid parameterization of the coarse resolution ocean model.

Plain Language Summary

This study applies a spatial coarse-graining method or a 2D spatial filter to define the subfilter or roughly speaking the mesoscale eddying structure as the deviation from the filtered large-scale field. Then, the Reynolds' temporal average is used to divide the eddying effect into transient and stationary parts. Leonard's decomposition further allows us to categorize the interactions of eddies versus large-scale flow. Both decompositions together with the flux-gradient relation, which links the eddy flux with the large-scale background gradient through either the isotropic transport coefficient or anisotropic transport tensor, help provide insights into mesoscale eddy transport parameterization design.

1 Introduction

Ocean physical processes with a horizontal spatial scale of approximately 50-500 km or near the first baroclinic Rossby deformation radius are usually called ocean mesoscale motions, including mesoscale eddies and meander structures. Mesoscale motions, which contain more than 80% of the ocean kinetic energy, impact ocean material transport, momentum budget, and interaction with large-scale and submesoscale ocean circulation. Therefore, resolving or at least parameterizing the oceanic mesoscale process in a numerical model is necessary. Since the milestone work of Gent and McWilliams (1990) and Gent et al. (1995) which proposed the GM parameterization scheme to mimic holistic eddy transport effect and the process of releasing the available potential energy by baroclinic instability for application in a coarse resolution ocean model, mesoscale eddy transport parameterization and its accompanying diagnostic methods and theories have been continuously developed over the past three decades, (e.g., McDougall & McIntosh, 1996; Treguier et al., 1997; Visbeck et al., 1997; Dukowicz & Smith, 1997; Griffies et al., 1998; Griffies, 1998; Marshall et al., 1999; Mcdougall & Mcintosh, 2001; Nakamura, 2001; R. Smith & Gent, 2004; Berloff, 2005; Cessi, 2007; Eden & Greatbatch, 2008; Ferrari & Nikurashin, 2010; Marshall et al., 2012; Hallberg, 2013; Bachman & Fox-Kemper, 2013; Bachman et al., 2015; Lu et al., 2016; Mak et al., 2017; Bachman, 2019; Haigh et al., 2020; Groeskamp

et al., 2020; Z. Stanley et al., 2020; Wei & Wang, 2021; Haigh & Berloff, 2021; Haigh et al., 2021a, 2021b, and others)

However, many current parameterization schemes for ocean mesoscale processes and related diagnostic methods have two major defects:

(I) The Reynolds' average method is often used for scale separation so that for any variable c, there is $\overline{\overline{c}} = \overline{c}$, $\overline{c'} = 0$. Nevertheless, the discrete grid algorithm of the numerical model does not necessarily meet the property of the Reynolds average. The grid discretization should be deemed as an implicit filter that one may not know the specific form (Germano et al., 1991; Germano, 1992), which is more likely to be represented by the spatial coarse-graining method. Under the coarse-graining method, $\overline{\overline{c}} \neq \overline{c}$, $\overline{c'} \neq 0$. If assuming a specific scale clearly separating the motion into two untangling parts (for example, the motion with a bimodal spectrum in spectral space), the coarse-graining method can be approximated as Reynolds' average. However, due to the continuity of the energy spectrum of ocean mesoscale processes (Aluie et al., 2018; Buzzicotti et al., 2021), the scale separation hypothesis cannot be well established. Therefore, the complete subgrid flux rather than the mere Reynolds term must be considered for oceanic eddy parameterization. In addition, the Reynolds term only includes the collective contribution of motions smaller than the separation scale (e.g. eddy-eddy interaction) to the larger scale. It does not incorporate the cross-scale or even multi-scale interactions.

(II) Most parameterization schemes only deal with the transient eddy process caused by instabilities, without explicitly involving topographic effect or stationary process which may significantly affect the eddy transport process. Many works (e.g., Treguier & McWilliams, 1990; Rintoul et al., 2001; MacCready & Rhines, 2001; Garabato et al., 2011; A. Thompson & Sallée, 2012; Bischoff & Thompson, 2014; Abernathey & Cessi, 2014; Radko & Kamenkovich, 2017; Youngs et al., 2017; Khani et al., 2019, and others) tried to establish the relationship between stationary phenomena and topography and how topography dynamically force the eddying processes. For example, stationary structures appear downstream of large-scale topographies, which cause zonal inhomogeneity of the flow, make a crucial contribution to the cross-front eddy mass and tracer transport, and both baroclinic instability and barotropic instability could play vital roles in these stationary structure dynamics(Youngs et al., 2017). Most relevant to our study, Lu et al. (2016) showed that stationary eddies would play a non-negligible role in eddy transport and the transport coefficient or tensor in the Southern Ocean (SO) so their effect should be involved in mesoscale eddy parameterization.

Given the above issues, this paper will leverage some large eddy simulation (LES) concepts to diagnose the eddy transport process and form a new perspective on the mesoscale eddy scheme. We believe LES is applicable to the current coarse-resolution climate models which have the typical horizontal resolution near or less than 1°(Hewitt et al., 2020). The grid scale is smaller than the largest mesoscale eddy in the ocean. Therefore, the parameterization of the subgrid process should consider the complete subgrid flux under the LES framework. This paper introduces Leonard's decomposition in LES to discuss the complete subfilter eddy flux and further develop Lu et al. (2016)'s stationary-transient eddy transport diagnostic framework. Using potential vorticity (PV) as a dynamical tracer, we apply this new framework to the realistic ocean data and numerical simulation results of the SO to investigate the characteristics of the subfilter transport in terms of 1) isotropic and anisotropic assumption, 2) stationary-transient decomposition and 3) Leonard's decomposition. This diagnostic framework of eddy transport not only distinguishes the contribution of stationary structure and transient motion in the SO and points out the importance of stationary process or topographic effect, but also looks into the collective effect of the interaction among small eddies, large eddies, and large-scale structures on a given spatio-temporal scale from the perspective of triad interaction, to provide theoretical support for better parameterizing mesoscale eddy process in ocean models. Section 2 will briefly review some basic concepts of the flux-gradient

relation, eddy transport tensor, isotropy, and anisotropy. We hybrid the spatial coarse-graining method and the temporal Reynolds' average to realize the stationary-transient decomposition, and introduce the so-called Leonard's decomposition in LES with its physical implication explained from the aspect of the triad interaction and Germano identity. This section also includes the data and some key processing methods in the calculation. Section 3 is the diagnosis results, in which Section 3.1 shows the results of subfilter eddy PV transport under the stationary-transient decomposition and Leonard's decomposition, Section 3.2 is the result of isotropic scalar transport coefficient, and Section 3.3 is for the anisotropic transport tensor, focusing on the eigenvalue analysis of its symmetric part. Section 4 is for conclusion and discussion.

2 Methods

2.1 The flux-gradient relation

Starting from the freely evolving dynamic tracer PV equation with the following form,

$$\frac{\partial q}{\partial t} + \nabla \cdot (\mathbf{u}q) = 0 \tag{1}$$

After the scale separation, we obtain the large-scale PV equation,

$$\frac{\partial \{q\}}{\partial t} + \nabla \cdot (\{\mathbf{u}\}\{q\}) + \nabla \cdot \mathbf{F_{sfs}} = 0 \tag{2}$$

where { } represents a certain scale separation operator with a smoothing effect and the subfilter eddy flux (or transport) is as follows.

$$\mathbf{F_{sfs}} \equiv \{\mathbf{u}q\} - \{\mathbf{u}\}\{q\} \tag{3}$$

In Appendix A, we introduce Germano identity (Germano et al., 1991; Germano, 1992) to distinguish the two concepts of subgrid and subfilter scale. We also point out in Appendix A that only when the separation scale of the explicit spatial coarse-graining filter is sufficiently larger than the scale of the implicit data resolution filter, the subfilter scale quantity obtained is valid and the subfilter flux would be regarded as the subgrid flux of a certain coarse-resolution model.

Suppose linear relation between the subfilter flux and large-scale PV gradient, namely adopt the flux-gradient relation as turbulent closure (Taylor, 1922; Vallis, 2017),

$$\mathbf{F_{sfs}} = -\mathbf{K}\nabla\{q\} \tag{4}$$

$\mathbf{K}$ is the eddy transport tensor of second-order, storing the local relation between the flux and the gradient in physical space. In the z-coordinate, $\mathbf{K}$ is a 3×3 tensor. However, the mesoscale motion away from the mixing layer is quasi-adiabatic and in principle along the neutral density surface or the minimum disturbance surface (McDougall, 1987; Fox-Kemper et al., 2013), so the process can be simplified to 2D. Then $\mathbf{K}$ becomes a 2×2 tensor.

The transport tensor needs not to be symmetric, and one may take symmetric-antisymmetric decomposition as follows,

$$\mathbf{A} \equiv \frac{1}{2}\left(\mathbf{K} - \mathbf{K}^T\right) \tag{5}$$

$$\mathbf{S} \equiv \frac{1}{2}\left(\mathbf{K} + \mathbf{K}^T\right) \tag{6}$$

$$\mathbf{F_{sfs}} = -(\mathbf{A} + \mathbf{S})\nabla\{q\} \tag{7}$$

The antisymmetric part $\mathbf{A}$ represents the skew advection along large-scale tracer contours, which corresponds to GM Scheme (Gent & McWilliams, 1990; Gent et al., 1995; Griffies et al., 1998; Griffies, 1998). The symmetric part $\mathbf{S}$ represents the Fickian-like diffusive process, which corresponds to Redi Scheme (Redi, 1982; Griffies et al., 1998; Griffies, 1998).

Further, diagonalize the symmetric tensor to get the eigenvalue matrix $\mathbf{\Lambda}$ and eigenvector matrix $\mathbf{V}$ as follows,

$$\mathbf{S} = \mathbf{V}^T \mathbf{\Lambda} \mathbf{V} \tag{8}$$

$$\mathbf{\Lambda} = \begin{bmatrix} \lambda_1 & 0 \\ 0 & \lambda_2 \end{bmatrix} \tag{9}$$

We call the larger eigenvalue λ_1 the major eigenvalue, the smaller λ_2 the minor eigenvalue. They represent the diffusion intensity along the major axis (parallel to the direction of the major eigenvector) and the minor axis (parallel to the direction of the minor eigenvector), respectively. $\lambda_1 \neq \lambda_2$ means anisotropic diffusion. $\lambda_1 = \lambda_2$ means isotropic diffusion. If the eddy transport process itself is purely isotropic, then the transport tensor collapses to the scalar coefficient κ and we have the flux-gradient relation

$$\mathbf{F_{sfs}} = -\kappa \nabla \{q\} \tag{10}$$

The transport coefficient here can be understood as the "efficiency" of the eddy transport process, that is, the length of the eddy flux vector standardized by the length of the large-scale PV gradient, or how much eddy transport can be excited under the background tracer field gradient of unit intensity.

Our diagnostic framework will be used to examine not only the eddy transport itself but also the isotropic transport coefficient and the anisotropic transport tensor.

2.2 The stationary-transient and Leonard's decomposition

This section introduces two independent decomposition methods of the subfilter flux and its transport tensor: the stationary-transient decomposition and Leonard's decomposition.

Like Lu et al. (2016), we use a 2D boxcar filter for spatial coarse-graining and Reynolds' temporal average to implement the stationary-transient decomposition. Any quantity c can be expressed as the sum of large-scale instantaneous background field, subfilter stationary eddying field, and subfilter transient eddying field, namely

$$c = [c] + c^* = [c] + \overline{c^*} + c^{*\prime} \tag{11}$$

where $[c]$ is for the spatial smoothed field; $\overline{c}$ is for the time-averaged field; $c^* = c - [c]$ is for the spatial subfilter eddying field, namely the original field minus the spatial smoothed field; $c' = c - \overline{c}$ is for the temporal eddying field, namely the original field minus the time-averaged field. The spatial subfilter eddying field c^* contains the stationary eddying field $\overline{c^*}$ and the transient eddying field $c^{*\prime}$. Note that the filter scale involved in this paper is 1°- 3° and inside the spectral range of the ocean mesoscale process. Although closely related, the subfilter scale cannot be completely equivalent to the oceanic mesoscale. If the mesoscale eddies are divided into large eddies and small eddies, the subfilter scale in this paper can be regarded as the ensemble of small eddies plus part of large eddies, and the filter scale can be regarded as the remaining part of large eddies plus large-scale field.

Replace the scale separation operator { } in in Eq.1 with $\overline{[\ ]}$, the subfilter PV flux becomes the following form

$$\mathbf{F_{sfs}} \equiv [\overline{\mathbf{u}q}] - [\bar{\mathbf{u}}][\bar{q}] \tag{12}$$

We now introduce the classical Leonard's decomposition in LES to decompose the subfilter flux.

$$\mathbf{F_{sfs}} = (\overline{[[\mathbf{u}][q]]} - [\bar{\mathbf{u}}][\bar{q}]) + (\overline{[[\mathbf{u}]q^*] + [\mathbf{u}^*[q]]}) + (\overline{[\mathbf{u}^* q^*]}) \tag{13}$$

The three terms in brackets on the right side of the equation are the Leonard term, Cross term, and Reynolds term, respectively (Leonard, 1974; Clark, 1977; Clark et al., 1979; Speziale, 1985; Germano, 1992; Fox-Kemper & Menemenlis, 2008; Anderson & Domaradzki, 2012). These three terms represent three categories of microstructures in the spectral space in terms of triad interaction (see Appendix B for details): 1) the Leonard term (combined with the large-scale transport term in the second term on the left of Eq.1) incorporates the collective effect of the triad interaction larger than the separation scale, which is defined as filtered-filtered or resolved-resolved interaction (including large-scale process, part of large-eddy versus large-scale flow interaction and part of large-eddy versus large-eddy interaction); 2) The Cross term represents the collective effect of the cross-scale interaction between the filtered and subfilter quantities on the filtered scale evolution, which is defined as filtered-subfilter or resolved-subgrid interaction (including eddy versus large-scale flow interaction, small-eddy versus large-eddy interaction and part of large-eddy versus large-eddy interaction); 3) The Reynolds term represents the collective effect on the filtering scale evolution caused by the process that occurs purely less than the separation scale, which is defined as subfilter-subfilter or subgrid-subgrid interaction (including the remaining eddy-eddy interaction that can be resolved by the data resolution). The collective effect here refers to the statistical effect on both large time and spatial scales. The essential difference between the three terms is that their triad elements have 0, 1, and 2 subfilter wave vectors, respectively. Since we do not choose the spectral truncated filter, the so-called "separation scale" above should be regarded as a generalized "separation scale or wavenumber interval" near the characteristic scale or wavenumber of the filter. In this interval, from larger scale to smaller scale, the proportion of subfilter components increases and tends to 1, and the proportion of filtered components gradually tends to zero. In addition, when the filter scale increases, the filtered part accommodates fewer eddying processes, so the Leonard term tends to be the pure large-scale process. Despite this expected dependence, our results will show that the qualitative behavior of Leonard's decomposition is not sensitive to the filter scale in the range we discussed.

Combine the stationary-transient decomposition with Leonard's decomposition, we have

$$\begin{aligned} \mathbf{F_{Lnrd,ttl}} &\equiv \overline{[[\mathbf{u}][q]] - [\mathbf{u}][q]} \\ &= ([[\bar{\mathbf{u}}][\bar{q}]] - [\bar{\mathbf{u}}][\bar{q}]) + ([\overline{[\mathbf{u}']}[\overline{q'}]]) \\ &= \mathbf{F_{Lnrd,stt}} + \mathbf{F_{Lnrd,trs}} \end{aligned} \tag{14}$$

$$\begin{aligned} \mathbf{F_{Crs,ttl}} &\equiv \overline{[[\mathbf{u}]q^*] + [\mathbf{u}^*[q]]} \\ &= ([[\bar{\mathbf{u}}]\bar{q}^*] + [\bar{\mathbf{u}}^*[\bar{q}]]) + ([\overline{[\mathbf{u}']}\overline{q^{*\prime}}] + [\overline{\mathbf{u}^{*\prime}[q']}]) \\ &= \mathbf{F_{Crs,stt}} + \mathbf{F_{Crs,trs}} \end{aligned} \tag{15}$$

$$\begin{aligned} \mathbf{F_{Rynlds,ttl}} &\equiv \overline{[\mathbf{u}^* q^*]} \\ &= [\bar{\mathbf{u}}^* \bar{q}^*] + [\overline{\mathbf{u}^{*\prime} q^{*\prime}}] \\ &= \mathbf{F_{Rynlds,stt}} + \mathbf{F_{Rynlds,trs}} \end{aligned} \tag{16}$$

The first terms on the right of the above three equations represent the stationary component, and the seconds are the transient ones. We use ttl, stt, and trs to represent the

total, stationary and transient components, respectively. The stationary and transient subfilter flux can be expressed as

$$\mathbf{F_{sfs,stt}} \equiv ([[\bar{\mathbf{u}}][\bar{q}]] - [\bar{\mathbf{u}}][\bar{q}]) + ([[\bar{\mathbf{u}}]\bar{q}^*] + [\bar{\mathbf{u}}^*[\bar{q}]]) + ([\bar{\mathbf{u}}^*\bar{q}^*]) \tag{17}$$

$$\mathbf{F_{sfs,trs}} \equiv ([[\overline{\mathbf{u}'}][\overline{q'}]]) + ([[\overline{\mathbf{u}'}\overline{q^{*\prime}}] + [\overline{\mathbf{u}^{*\prime}[q']}]]) + ([\overline{\mathbf{u}^{*\prime}q^{*\prime}}]) \tag{18}$$

The stationary part is composed of time-averaged quantities. It captures the time-invariant or slowly-varying imprint, which is forced by setting system boundary conditions (such as topography and air-sea flux) and hyperparameters (such as the Coriolis parameter f and β). The transient part measures the collective effect of the evolving dynamic adjustment processes around the stationary structure in the system.

Through the flux-gradient relationship, we can obtain the transport tensor for every part,

$$\mathbf{F_{sfs}} = -\mathbf{K^{sfs}}\nabla[\bar{q}] \tag{19}$$

$$\mathbf{F_{stt}} = -\mathbf{K^{stt}}\nabla[\bar{q}], \quad \mathbf{F_{trs}} = -\mathbf{K^{trs}}\nabla[\bar{q}] \tag{20}$$

$$\mathbf{F_{Lnrd}} = -\mathbf{K^{Lnrd}}\nabla[\bar{q}], \quad \mathbf{F_{Crs}} = -\mathbf{K^{Crs}}\nabla[\bar{q}], \quad \mathbf{F_{Rynlds}} = -\mathbf{K^{Rynlds}}\nabla[\bar{q}] \tag{21}$$

We also have the expressions of the transport tensors,

$$\mathbf{K^{sfs}} = \mathbf{K^{stt}} + \mathbf{K^{trs}} = \mathbf{K^{Lnrd}} + \mathbf{K^{Crs}} + \mathbf{K^{Rynlds}} \tag{22}$$

namely, the transport tensor can also be decomposed by the stationary-transient and Leonard's decomposition. So far, we have established a multifaceted eddy transport diagnosis framework using both the stationary-transient and Leonard's decomposition as well as whether isotropic or not. This framework helps investigate the contribution of the stationary and transient effects and different categories of triad interaction under Leonard's decomposition to the eddy transport in the SO.

2.3 Data and processing method

The main results of this paper are based on the five-day average SOSE eddy-permitting data (Mazloff et al., 2010) with a horizontal resolution of 1/6° in 2008. Data from an eddy-rich quasi-global model LICOM2 (LASG/IAP Climate system Ocean Model) with a horizontal resolution of 1/10° is used for validation (see Yu et al. (2012) for the simulation setting). We take the data in the 63rd model year, which is well spinup. The study area is south of 25°S. In this paper, the temporal Reynolds' average is the annual average, and the spatial coarse-graining adopts the boxcar filter with a fixed size of 2°. We will also show some results of 1° and 3° to discuss the sensitivity to the selected separation scale, but the major discussion is for 2°. When close to the boundary, the filter size remains unchanged, and the missing values are set to zero to participate in the filtering, so the filtered boundary also becomes fuzzy. This method performs well in terms of energy conservation and commutes with differential operators (Buzzicotti et al., 2021), and its discretization expression is as follows,

$$[c]_{mn} = \frac{1}{num}\sum_{i=m-ir}^{m+ir}\sum_{j=n-ir}^{n+ir} w_{ij}c_{ij}, \quad num = (2ir+1)^2 \tag{23}$$

ir is the gird number of half filter size, and w_{ij} is the area weight.

The multifaceted diagnostic framework of this paper needs to be carried out on the neutral density surface. We use the topobaric surface to estimate the neutral surface, which is highly accurate (Stanley, 2019). We choose the surface with a neutral density of $36.8kg/m^3$ for discussion because it has outcrop areas near the Antarctic continent only a few times a year. In most areas north of 60°S, its depth is about $1500\pm1000m$, enabling us to reduce the influence of the diabatic process in the mixing layer. The results of flux and transport tensor in other layers are qualitatively consistent. In addition, the potential density $\sigma 2$ can also be used to estimate the neutral density, which is significantly different from the results of the topobaric surface in places with steep isopycnal slope (such as the ACC core) near the outcrop area. However, the spatial distribution of physical quantities in other places is qualitatively consistent. To reduce the amount of calculation, we only processed higher resolution LICOM data on the $\sigma 2$ plane. The velocity field under this framework is the velocity projected from the z-coordinate to the neutral plane. The dynamic tracer PV, $q = fN^2/g = -\frac{f}{\rho}\frac{\partial \rho}{\partial z}$, is firstly calculated in the z-coordinate and then interpolated into the neutral coordinate. Appendix C gives a brief example of our interpolation algorithm. The subsequent filtering and gradient operations are carried out on the neutral plane.

On the neutral plane, the total subfilter PV flux is calculated first, and then the components of the flux are obtained through the stationary-transient and Leonard's decomposition. Then the corresponding transport tensors or coefficients are estimated through the flux-gradient relation. Finally, the transport tensors are decomposed into symmetric and antisymmetric parts, and the eigenvalues and eigenvectors of the symmetric tensor are calculated. Unlike the multi-tracer method (Bachman et al., 2015), only one dynamic tracer is used here. We carried out the least-square regression of neighboring samples to solve the underdetermined problem in estimating the transport coefficient or tensor. Appendix C describes how the approach is implemented. Specifically, solving the transport tensor is equivalent to solving the following binary linear least-square regression problems,

$$\begin{bmatrix} f^x \\ f^y \end{bmatrix} = \begin{bmatrix} K_{xx} & K_{xy} \\ K_{yx} & K_{yy} \end{bmatrix} \begin{bmatrix} [\bar{q}]_x \\ [\bar{q}]_y \end{bmatrix} \rightarrow \begin{cases} f^x = K_{xx}[\bar{q}]_x + K_{xy}[\bar{q}]_y \\ f^y = K_{yx}[\bar{q}]_x + K_{yy}[\bar{q}]_y \end{cases} \tag{24}$$

f^x and f^y are the zonal and meridional subfilter PV flux, respectively. The estimation of the isotropic coefficient is also similar and becomes linear least-square regression between the length of flux vector and the length of the large-scale PV gradient vector.

3 Result

3.1 Meridional subfilter PV flux

3.1.1 The stationary-transient decomposition

As show in Figure C1a The large value area of the meridional subfilter PV flux is concentrated in the south of the domain and the eastern side of the continent or submarine plateau (Figure C1a and C1g). The large value zone near the Antarctic continent reflects the influence of non-conservative processes such as sea-ice dynamics, and outcropping of the neutral surface or mixing layer effect. Since our framework is designed for inner ocean quasi-adiabatic motion, we will not discuss this more but blame it on the inapplicability of our diagnostic method there. The large value zones on the eastern side of large-scale topography have clear physical significance. They are contributed mainly by the stationary flux (Figure C1b), so it reflects the anchoring effect of topography on the eddy transport pattern. In addition, the mid-ocean ridge imprint a clear pattern on both stationary and transient subfilter flux, which is manifested in the arc-shaped magnitude mutation area near 150°E-150°W, 60°S and 10°E-35°E, 50°S and the northward extension of the large value area at 80°E, 150°E and 10°W. Our results reflect the duality of the topographic effect, that is, the large-scale topography not only anchors stationary structures of the flux field but also organizes transient adjustment processes nearby.

This is consistent with previous studies using idealized models or observation data to diagnose eddy kinetic energy, eddy momentum flux, eddy buoyancy flux, and other eddy tracer fluxes (e.g., A. Thompson & Sallée, 2012; A. Thompson & Garabato, 2014; Bischoff & Thompson, 2014; Youngs et al., 2017). In addition, although the results of boxcar filters of different sizes are qualitatively consistent (Figure S1), the separation scale would affect the relative contribution of the stationary and transient components to the subfilter flux (Figure C3). The larger the filter scale, the stronger the contribution of the stationary part and the weaker the transient part. This is because the high-pass field with a larger filter scale contains more large-scale information. The dominance of the stationary part increasing with the filter size reflects that the scale of the transient process is smaller than the scale of the stationary structure formed by the anchoring effect of the topography. An example is that the quasi-stationary meander in the SO is often larger than the transient mesoscale eddy (Williams et al., 2007; Chapman et al., 2015).

3.1.2 Leonard's decomposition

This section investigates the Leonard term, Cross term, and Reynolds term of the subfilter flux under Leonard's decomposition. From the horizontal distribution and probability density function (PDF) of meridional PV flux (Figure C2 and C3), we find large a Leonard term and Cross term with a positive and negative staggered wave train distribution in the domain. However, there is a violent offset between the two, which makes the sum term one order of magnitude smaller than the individual term but still stronger than the Reynolds term holistically (Figure C3). Similarly, when Galmarini et al. (2000) used the high-frequency time series of atmospheric variables for time coarse-grained analysis, they also observed significant Leonard term and Cross term and their partial cancellation. Speziale (1985) pointed out that the complete subfilter eddy flux, the sum of the Leonard term and Cross term, and the individual Reynolds term all satisfy Galilean invariance, but the form of the individual Leonard term or Cross term is not Galilean invariant. Therefore, he suggested that the Leonard and Cross term should be parameterized together, and the Reynolds term should be parameterized separately. We are not sure whether the offset here is related to the breaking of Galilean invariance. Most existing mesoscale eddy parameterization schemes are theoretically derived based on Reynolds' average. Only the Reynolds term is included, and the other two terms under Leonard's decomposition are missed. The results here at least show the importance of considering a complete subgrid flux, which incorporates the resolved-resolved, resolved-subgrid, and subgrid-subgrid interactions, and selecting appropriate parameterization form for different processes when designing eddy transport parameterization.

In addition, these three terms are dominated by the stationary part, and the offset between the Leonard and Cross term is mainly from their stationary components. From Eq.14 of the Leonard term, one may also regard it as a standing wave with asymmetric amplitude. The geographical position of the peaks, troughs, and zeroes is quasi-fixed. The stationary Leonard term is the spatial distribution of a stationary background state with systematic amplitude shift relative to the zero axis just like a canvas with inhomogeneous background color. The transient Leonard term is the collective effect of the disturbances that only time-dependent modifies the amplitude of the standing wave. The stationary Cross term may be understood as a tendency to excite the cross-scale or multi-scale interaction in specific geographical locations through many possible mechanisms. For example, the western boundary flow is the graveyard of eddies (Zhai et al., 2010). The eddy may also tend to extract energy from the background flow at a specific location near topography (Abernathey & Cessi, 2014; A. Thompson & Garabato, 2014). Special geometric shapes and configuration of eddy and background flow to realize cross-scale energy conversion (Waterman & Lilly, 2015; Youngs et al., 2017), which might repetitively occur someplace, would also contribute to the stationary Cross term.

Further comparing the results of SOSE with higher resolution LICOM simulation (Figure S2), the spatial distribution of the Leonard or Cross term from different data is qualitatively consistent in terms of wavelength and geographical distribution of the wave train structure. Therefore, one speculation is that these two reflect the system's fingerprint under the current topographic and climate state or model setting. Since the stationary part dominates these two, we offer an interpretation of the wave train structure that macro-conditions of the system, such as all its boundary conditions (e.g. topography and air-sea flux) and hyperparameters (for example, f and β), can decisively stimulate the large-scale process, eddy versus large-scale interaction and small eddy versus large eddy interaction encompassed in the Leonard and cross term with a definite geographical distribution.

3.2 The isotropic transport coefficient

3.2.1 The stationary-transient decomposition

The large values of the isotropic subfilter transport coefficient (Figure C1d) are mainly in the vigorous flow areas, such as the Antarctic Circumpolar Current (ACC), the Agulhas retroflection, and the Malvinas current. Under the stationary-transient decomposition (Figure C1def), the stationary coefficient dominates in most places, and the large transient coefficient mainly concentrates in the most energetic flow area such as the ACC. This is a surprising result. Although some studies, for instance, Lu et al. (2016) has discovered the significance of the stationary part in the transport process, we uncover for the first time that the stationary effect would dominate the transport process when the complete subfilter flux is considered, so a complete mesoscale eddy scheme should never omit the stationary effect. Large-scale topography often excites strong subfilter transport coefficients downstream of the local flow, such as the eastern side of the Kerguelen plateau and Campbell Plateau, the Malvinas current, and the southwest side of the African continent which is equivalent to the downstream of the Agulhas retroflection. In addition, the coefficient also has the structure of several banded weak value areas, which is particularly obvious in the stationary part at 100°E-160°W. This structure may be related to the mid-ocean ridge because its orientation is consistent with the mid-ocean ridge. The topographic type of large-scale and undulating zonal ridges can form an obstacle to eddy mixing by locally strengthening the jet (A. F. Thompson, 2010). In observation data or realistic model runs, the role of topography on the flow field is a complex, multi-scale problem. This work only qualitatively sheds some light on the influence of topography on the eddy transport process. Future work will comprehend how the specific topographic configuration drives the transport under our diagnostic framework by carrying out idealized numerical experiments with a simplified model setting. In addition, the size of the boxcar filter affects the relative contribution of the stationary and transient components to the subfilter transport coefficient: the larger the filter scale, the more the contribution of the stationary part (Figure C5).

3.2.2 Leonard's decomposition

The relative magnitude among the three terms of the subfilter eddy transport coefficient is consistent with the subfilter flux result when Leonard's decomposition is adopted. The Leonard and Cross term is one order of magnitude larger than the Reynolds term, and they partially offset each other but the sum of the Leonard and Cross term is still more intense than the Reynolds term (Figure C5). The Leonard term and Cross term achieve high intensity on the ACC core and its northern flank, while their magnitude drops drastically on the southern side of ACC (Figure C4). Compared with Figure C1g, the continuous submarine plateau, mid-ocean ridge between 50°S and 70°S shape the boundary of different levels of intensity of the Leonard and Cross transport coefficient. In addition, although the subfilter flux and the Reynolds transport coefficient are small in the gyre area (such as 40°S in the South Pacific) where the flow is relatively slow and EKE

is not that vigorous, the Leonard and Cross coefficient reach a decent level of intensity. This means the standing wave effect and cross-scale interaction represented by the Leonard and Cross transport coefficients are of high efficiency influencing tracer transport dynamics. Classical schemes are often based on Reynolds' average assumption, so they merely handle the effect of the Reynolds term, not the full transport process. The Leonard and Cross effects are overwhelming in areas where mesoscale eddy activity is not abundant, and they should be taken into account when parameterizing.

Although the diagnosis of the isotropic transport coefficient is instructive, the transport coefficient in this paper attempts to establish the association between the length of large-scale PV gradient and flux. In its mathematical essence, the isotropic form blends information from different directions. That leads to a dramatic error of meridional PV flux reconstructed by the isotropic transport coefficient (Figure C6bc), and the failure to capture the stationary PV flux field pattern inscribed by the topographic anchoring effect. However, if the anisotropic transport tensor is used, the reconstruction error can be greatly reduced (Figure C6de). As a second-order tensor, the anisotropic transport tensor stores more critical dynamic connections, especially the topographic effect exerted in different orientations, than the isotropic coefficient which is a zero-order tensor. Therefore, we will discuss the anisotropic framework in the next section.

3.3 The anisotropic transport tensor

The anisotropic transport tensor can be decomposed into a symmetric and antisymmetric tensor. The symmetric part represents the Fickian-like eddy diffusion process, and the antisymmetric part represents the advective process of skew flux (Griffies et al., 1998; Griffies, 1998). Although our diagnostic framework can generate the results of all relevant components and elements of the transport tensor, we only focus on the eigenvalues of the symmetric tensor (hereinafter referred to as the transport eigenvalues). The results of the antisymmetric part are given in Figure S8, but will not be discussed in this manuscript.

3.3.1 The transport eigenvalues

The transport eigenvalue has features qualitatively consistent with the transport coefficient above, including: 1) the large value of the subfilter transport eigenvalue is concentrated in the vigorous flow region, and the contribution of the stationary part is stronger than that of the transient part (Figure C7 and C8). 2) The eigenvalue intensity of the Leonard and cross terms is at least one order of magnitude greater than that of Reynolds terms (Figure C8), but the eigenvalues of these two terms do not seem to offset. In fact, when considering the subfilter flux and transport coefficient, the coordinate axes of the vector projection are meridional and zonal. However, in the eigenvalue analysis, the base vectors are the local major eigenvector and minor eigenvector, so the eigenvalues of the Leonard and cross term do not have additivity. 3) The Leonard and Cross term are completely dominated by the stationary part (Figure S4, S5 and C8), and the stationary and transient part of the Reynolds term are nearly in the same order of magnitude (Figure S3 and C8). As the spatial separation scale decreases, the importance of the transient part increases (Figure S7); When the eddy-rich LICOM data is adopted for a fixed spatial separation scale, the importance of the transient part also increases (Figure S6). 4) The transport eigenvalue intensities of the Leonard and cross terms have a distinct boundary near 60°S. As mentioned above, this boundary is related to the separation of bottom topography. There is a decent level of eigenvalue intensity where the flow is relatively weak in the northern flank of ACC.

In addition to the above features, the transport eigenvalues can better show the anchoring effect of the topography, especially the minor eigenvalues of the stationary Reynolds term are strengthened on the eastern side of all large-scale topography (Figure S3e). This indicates that 1) the response of the transport process to topographic forcing has distinct directionality, and 2) the anisotropic transport tensor can distinguish the physical relationship in different directions.

We next discuss the unique characteristics of the transport eigenvalue, that is, the three combinations of the transport eigenvalues, including 1) positive major eigenvalue and negative minor eigenvalue (major+, minor-), 2) positive eigenvalues (major+, minor+), and 3) negative eigenvalues (major-, minor-). We will try to uncover the phenomena in realistic data and the physical implication.

From the large-scale PV equation Eq.2, we can obtain the large-scale PV enstrophy equation,

$$\frac{\partial}{\partial t}\left(\frac{\{q\}^2}{2}\right) + \{q\}\nabla\cdot(\{\mathbf{u}\}\{q\}) + \nabla\cdot(\{q\}\mathbf{F_{sfs}}) - \mathbf{F_{sfs}}\cdot\nabla\{q\} = 0 \tag{25}$$

We can further get the domain-integrated equation and focus on the terms incorporating the subfilter process,

$$\frac{\partial}{\partial t}\int_\Omega \frac{\{q\}^2}{2}d\Omega \sim -\int_\Omega \nabla\cdot(\{q\}\mathbf{F_{sfs}})\,d\Omega + \int_\Omega \mathbf{F_{sfs}}\cdot\nabla\{q\}d\Omega \tag{26}$$

$$Z = \int_\Omega \frac{\{q\}^2}{2}d\Omega \tag{27}$$

Here Z is the domain integral of large-scale PV enstrophy, hereinafter referred to as large-scale enstrophy. Under the condition that the boundary value is zero (the coarse-graining method in this paper makes the large-scale PV asymptotically close to zero at the domain boundary), the first term on the right of Eq.26 is zero, then we obtain the following relation,

$$\frac{\partial Z}{\partial t} \sim \int_\Omega \mathbf{F_{sfs}}\cdot\nabla\{q\}d\Omega = -\int_\Omega \mathbf{K}\nabla\{q\}\cdot\nabla\{q\}d\Omega = -\int_\Omega \mathbf{S}\nabla\{q\}\cdot\nabla\{q\}d\Omega \tag{28}$$

Note that the antisymmetric tensor $\mathbf{A}$ is eliminated because its skew flux is perpendicular to the large-scale PV gradient. For the interaction of symmetric tensor $\mathbf{S}$ and PV gradient vector, we consider coordinate rotation to transform from local $x-y$ coordinate (i.e. the base vector is the local zonal and meridional unit vector) to local characteristic coordinate $v_1 - v_2$ (i.e. the base vector is two local eigenvectors),

$$\mathbf{S}\nabla\{q\} = \begin{bmatrix} S_{xx} & S_{xy} \\ S_{yx} & S_{yy} \end{bmatrix}_{x,y} \begin{bmatrix} r_x \\ r_y \end{bmatrix}_{x,y} \tag{29}$$

$$= \begin{bmatrix} \lambda_1 & 0 \\ 0 & \lambda_2 \end{bmatrix}_{v_1,v_2} \begin{bmatrix} r_{v_1} \\ r_{v_2} \end{bmatrix}_{v_1,v_2} = \begin{bmatrix} \lambda_1 r_{v_1} \\ \lambda_2 r_{v_2} \end{bmatrix}_{v_1,v_2} \tag{30}$$

r_x and r_y are the projections of the large-scale PV gradient vector in the x and y direction respectively, and r_{v1} and r_{v2} are the projections of the gradient vector in the major and minor eigenvector direction, respectively. Note that the tensor and vector themselves are invariant under a coordinate transformation. The first and last expressions represent exactly the same objective entity, but their projection's expression changes in different coordinates.

Finally, we obtain the eigenvalues' contribution to large-scale enstrophy as

$$\frac{\partial Z}{\partial t} \sim -\int_\Omega \mathbf{S}\nabla\{q\}\cdot\nabla\{q\}d\Omega = -\int_\Omega \left(\lambda_1 r_{v_1}^2 + \lambda_2 r_{v_2}^2\right)d\Omega \tag{31}$$

(major+, minor-) represents the attenuation of the large-scale PV enstrophy in the major characteristic direction and the enhancement of enstrophy in the minor direction, corresponding to the vortex filamentation process (Haigh et al., 2020; Ledwell et al., 1998); (major+, minor+) weakens the large-scale PV enstrophy in both characteristic directions, which means a pure sink of the enstrophy, and the anisotropy implies that the rates in different directions are different; (major-, minor-) enhances the large-scale PV enstrophy, meaning a pure source of enstrophy. (major+, minor-) is the most common case (Figure C7). The joint PDF of eigenvalues is mainly concentrated in the fourth quadrant (Figure C8), and the occurrence frequency is more than 70% (Figure C9a), which means that the vortex filamentation process is dominant in the subfilter transport process in the SO. This result is consistent with Haigh et al. (2020); Haigh and Berloff (2021); Haigh et al. (2021b); Kamenkovich et al. (2021), but their results are obtained from studying instantaneous transport eigenvalues of a closed ocean basin. The other two cases' frequency under different terms has different behavior (Figure C9a), specifically (1) the frequency of (major+, minor+) of total subfilter, total Reynolds, stationary subfilter, stationary Reynolds, and all transient terms are higher than that of (major+, minor-), indicating that the pure sink area of the large-scale PV enstrophy caused by the transient process and subfilter-subfilter interaction in the SO is larger than the pure source area; (2) The frequency of total and stationary Leonard and cross terms is almost the same, indicating that the pure source area and pure sink area of the large-scale PV enstrophy formed by standing wave effect and stationary cross-scale interaction in the SO are nearly the same.

To explore the anisotropy of transport eigenvalues, unlike Rypina et al. (2012) and Bachman et al. (2020) which used tensor ellipses to visualize local anisotropy, we calculate the logarithm of the absolute value of the ratio of major and minor eigenvalues under all three eigenvalue combinations as a measure of anisotropy and focus on their statistical characteristics. In Figure C9b, we use boxplots to show their mean, 1-fold standard deviation of the mean, and the upper and lower 5% quantiles. For the case of (major+, minor+) (red box), the mean anisotropy of all terms is near 1, and the upper 5% quantile is at least 2, which indicates the major eigenvalue is at least one order of magnitude or even more than two orders of magnitude larger than the minor eigenvalue and dominates the degree of anisotropy in a considerable part of the domain. For the most common case of (major+, minor-) (green box), the mean anisotropy of all terms is near 0, and the 1-fold standard deviation of the mean falls within ± 1, indicating the magnitude of major and minor eigenvalues is close to each other. For the case of (major-, minor-) (blue box), the mean anisotropy of all terms is less than -1, and the lower 5% quantile significantly breaks through -2, which indicates the minor eigenvalues dominate the degree of anisotropy. In conclusion, the anisotropy of the eddy transport process in the SO is ubiquitous and drastic.

As for different terms, the boxplot of total and stationary Leonard and Cross terms is highly symmetric about the zero line; that is, the red box and blue box of Lnrd-ttl, Crs-ttl, Lnrd-stt, Crs-stt are symmetric about the zero line, while the green box itself is symmetrical about the zero line. The upper 5% quantile of the other eight terms with (major+, minor+) (the top of the red box) is slightly closer to the zero line than the lower 5% quantile of (major-, minor-), indicating that the anisotropy in the pure source of enstrophy formed by the standing wave effect and stationary cross-scale interaction is slightly greater than that in the pure sink. In addition, the mean value of the other eight terms with (major+, minor-) is greater than zero, and their upper 5% quantile is more distant from the zero line than their lower 5% quantile, indicating that the transient process, eddy-eddy interaction and vortex filamentation process in the SO slightly dissipate the large-scale PV enstrophy holistically.

3.3.2 The transport characteristic direction

This section will discuss the eigenvectors of the symmetric transport tensor. Since the major eigenvalue specified by the algorithm is always greater than or equal to the minor eigenvalue, when the major and minor eigenvalues are both negative, the major eigenvector is not in the dominant direction. Therefore, we select the major eigenvector where the absolute ratio of major and minor eigenvalues is greater than a threshold value α, and the minor eigenvector where the absolute ratio of major and minor eigenvalues is less than $1/\alpha$, to synthesize the truly dominant characteristic direction with strong anisotropy. We calculate the PDF of the angle between the dominant direction and the vector of the large-scale topographic slope, PV gradient, and velocity, as shown in Figure C10, and α is taken as 5. We find the dominant characteristic direction has a strong tendency to be perpendicular to the large-scale PV gradient and parallel to the large-scale velocity vector, and a weak tendency to be perpendicular to the large-scale topographic slope. This is consistent with the results diagnosed by Bachman et al. (2020) with global model data, indicating that the PV gradient barrier and shear dispersion mechanism are critical for the maintenance of anisotropy (Young et al., 1982; S. Smith, 2005; Srinivasan & Young, 2014; Bachman et al., 2020). We further explore the influence of the threshold α. in Figure C11, we investigate the angle between the dominant characteristic direction and the PV gradient when α is 2, 5, 10, and 20. With more intense anisotropy, the perpendicular tendency of the dominant characteristic direction and both its stationary and transient parts are significantly enhanced, with the stationary part's enhancement more dramatic.

Similarly, we can obtain the angles in the weak anisotropy area by giving the threshold γ, as shown in Figure C10, and set $\gamma = 2$. The angle between the dominant characteristic direction and the topographic slope or the velocity vector is almost random and evenly distributed, but the angle between the dominant characteristic direction and the PV gradient peaks near 50°. As the threshold γ (Figure C11) decreases or the isotropy increases, the PDF of the angle between the dominant direction and the PV gradient tends to be symmetrically distributed with 45° as the central peak. These phenomena mean no dominant mechanism among which we have studied can decide the eigenvector when the process is quasi-isotropic.

The tendency of the stationary dominant eigenvector to be perpendicular to the PV gradient or parallel to the velocity vector is much stronger than the transient component. But there is only a weak orthogonal tendency between the stationary dominant direction and the topographic slope. So it seems that the direct effect of topography is exerted more on the magnitude of transport-related quantities, not their direction.

Above we confirm the relationship between the dominant characteristic direction and the PV gradient under the constraint of geostrophic dynamics. At the same time, we further point out that in the region with high transport anisotropy, the dominant characteristic direction is more likely to be perpendicular to the PV gradient, indicating that the PV barrier mechanism would have a crucial impact on the eddy transport process (Ferrari & Nikurashin, 2010; Srinivasan & Young, 2014; Bachman et al., 2020).

4 Summary

This paper combines the stationary-transient decomposition and Leonard's decomposition in LES to form a multifaceted diagnostic framework for the eddy transport process applied in the SO. We not only distinguish the contribution of stationary structure and transient motion and validate the importance of stationary process or topographic effect, but also investigate the collective effects of the standing wave, cross-scale interaction, and subfilter eddy-eddy interaction on the filtered space-time scale from the perspective of triad interaction.

The discussions of scale separate filter, Leonard's decomposition, and Germano identity help form a new paradigm of viewing the subgrid transport process with the hope of being aligned with numerical model practice as much as possible. We emphasize the complete eddy flux and LES framework need to be considered in the subgrid parameterization of coarse resolution or even non-eddy resolving ocean general circulation model. That is, besides the collective effect of subgrid eddy-eddy interaction represented by the Reynolds term, the Leonard and cross terms should also be parameterized to compensate for the missing standing wave effect and cross-scale interaction. In addition to the aforementioned points, the diagnostics in this paper are isoneutral, so the problem is simplified into 2D, and the neighboring sampling regression method is used to solve the underdetermined problem of estimating the transport tensor or coefficient when using a single tracer. We also systematically investigate the performance of transport coefficients and transport tensors (mainly transport eigenvalues and eigenvectors) and the factors behind them under isotropy and anisotropy assumptions.

The main conclusions of this paper are as follows:

(1) From the stationary-transient decomposition, we found that the stationary effect cannot be ignored for subfilter eddy transport and is primarily determined by the geographical distribution of topography. Topography not only directly engraves the stationary structure of the PV flux field but also organizes the flow to generate transient adjustment processes near large-scale topography. As the spatial separation scale increases, the proportion of stationary contribution increases. This paper's two sets of data are qualitatively consistent in these characteristics.

(2) From Leonard's decomposition, we found that it is necessary to consider the complete subgrid flux. Although there is a significant cancellation between the Leonard and Cross term, the sum of Leonard and Cross term is at least as critical as the Reynolds term. Their stationary parts dominate both terms. The Leonard term may be considered as a large-scale standing wave effect, and the cross term represents the eddy-flow or small eddy versus large eddy interaction across the separation scale. They consist of several wave train structures and may reflect the system's fingerprint shaped by the current geological, climate state, or model settings.

(3) The transport coefficient establishes the relationship between the length of the background PV gradient and the PV flux length. In its mathematical essence, the information in different directions is mixed together, and the reconstructed meridional PV flux error is quite large. Instead, the anisotropic tensor greatly reduces the reconstruction error because of its ability to distinguish the directionality of dynamic information, especially the anisotropy of the topographic anchoring effect.

(4) The sign combination of the transport eigenvalues of the symmetric tensor represents its contribution to the large-scale PV enstrophy in the domain integral sense. All three cases occur in the SO, but in most regions the combination is (major +, minor -), which means the dominance of the vortex filamentation process in the SO, and the process slightly dissipates large-scale enstrophy holistically. The relative difference between the two eigenvalues links to anisotropy, and the eddy transport process in the SO is highly anisotropic. The anisotropy at the pure source is slightly greater than that at the pure sink. The stationary standing wave effect and cross-scale interaction tend to enhance the anisotropy. In the region with stronger anisotropy, the dominant characteristic direction is easier to be perpendicular to the large-scale PV gradient, indicating that the PV barrier mechanism would significantly enhance the anisotropy of the eddy transport process.

As a preliminary work, this study only focuses on establishing the research framework, data with higher resolution, and larger research areas should be selected for more in-depth research in the future. In terms of data resolution, we try to balance between

reducing the amount of calculation and ensuring sufficient resolution to study the filtering scale phenomenon. On the one hand, the resolution of the current non-eddy resolving or eddy-permitting ocean general circulation model can be less than 1°. According to the Germano identity, considering the implicit filter effect of resolution and sufficient buffer scale band, the data resolution used to approximate DNS needs to be at least 1/12°. In this sense, the results from our data and filter scale fail to directly provide quantitative suggestions for the eddy parameterization but only enlighten the possibility of a scheme more in line with the realistic oceanic eddy transport process, and attention should be paid to the qualitative characteristics diagnosed. On the other hand, using the highest resolution data nowadays (up to 1/50° or even higher) as close to DNS as possible can allow systematic exploration of the scale dependence of stationary-transient decomposition, Leonard's decomposition, and potential subgrid scheme in both spectral space and physical space, which will be a promising application of this framework. In addition, the temporal resolution and duration of the data in this paper only meet the minimum requirements. If climate research is carried out or submesoscale processes are considered, one should use long-time data or data with higher temporal resolution. The study area is limited to the SO and studying the other three ocean basins might lead to some new features.

In addition, some works (e.g., Haigh & Berloff, 2021; Haigh et al., 2021a, 2021b; Sun et al., 2021) used the divergent part of the eddy flux under the Helmholtz decomposition, because the net dynamic effect on the evolution of large-scale tracer field in equation (2) is the eddy flux divergence. However, when the domain is bounded, the result of the rotation-divergence decomposition of the flux is not unique, complicating the problem (Fox-Kemper et al., 2003; Bachman et al., 2015). Secondly, although some works, such as Maddison et al. (2015), have proposed some promising methods of implementing this decomposition, the definition of the boundary would be blurred after spatial coarse-graining (Buzzicotti et al., 2021), which makes it impossible to artificially specify the boundary conditions of rotational and divergent flux when solving the partial differential equation under the Helmholtz decomposition (in fact, only the complete flux on the boundary can be known) and would affect the result of divergent flux. In practice, it may be a more natural choice to obtain the original flux first, and then directly remove any non-divergence part through the divergence operator (Fox-Kemper et al., 2003). Finally, tracer transport has a clear and concise physical meaning connected with parcel excursion theory (Taylor, 1922; Bachman et al., 2015). Therefore, our diagnostic framework only discusses the original flux without the rotation-divergence decomposition.

To sum up, our framework should be regarded as a new tool or a new thinking paradigm for classifying, extracting, and integrating the information of complex eddy transport processes. It cannot directly specify the dynamic mechanism, so it must be combined with other theories to validate and explain the phenomenon. An example is the framework can reflect some characteristics of topographic effect but cannot directly describe the intermediate physical process or mechanism of how a specific type of topography exerts its influence. Therefore, further research on topographic effects based on our framework should be combined with well-designed idealized numerical experiments for our future work orientation.

Appendix A

Here we discuss the conceptual difference between the subfilter scale and subgrid-scale. In LES, Germano et al. (1991) and Germano (1992) proposed the so-called Germano identity,

$$\mathbf{F_{sfs}} \equiv \overline{\overline{\mathbf{u}}^G \overline{c}^G}^F - \overline{\overline{\mathbf{u}}^G}^F \overline{\overline{c}^G}^F \tag{A1}$$

$-G$ is an implicit filter with unknown expressions, such as the numerical grid discretization scheme or data resolution limit, and $-F$ is an explicit filter of a given specific form,

such as the boxcar filter used in this paper. The original variables should be the true fields or direct numerical simulation (DNS).

In this study, these two datasets used are not from DNS, so the implicit filter is the grid resolution limit of SOSE or LICOM. According to Germano identity, the subgrid-scale refers to scales missed or poorly described in the dataset. Information in scales smaller than grid scale is eliminated, and physical processes in a range of scales slightly larger than the grid resolution would be underestimated or misrepresented. Based on the experience that numerical simulation requires at least five or six grid points to capture a structure better, we assume that the ultimately influenced scale of an implicit filter would reach a spatial scale six times its resolution, for example, 1° for SOSE and 0.6° for LICOM. On the scales larger than the ultimately influenced scale, we suppose they can represent the physical processes in a relatively sound manner. Therefore, the data used in this paper are sufficient to study the part with a larger horizontal scale of the mesoscale processes, not small eddies, in the SO.

As for the explicit filter in Germano identity, the boxcar filter is used in this paper, which determines the so-called subfilter scale. Liu et al. (1994) systematically discusses the application of boxcar filter, Gaussian filter, and spectral truncation filter in LES. He found that using a boxcar filter and Gaussian filter can achieve a high correlation between the stress field predicted by LES and the observed stress field. Boxcar filter is not a clean truncation in spectral space [Fig. 4 of Ciofalo (1994)]. When it is smaller (greater) than the characteristic wavenumber (spatial scale) of the filter, the boxcar filter's Fourier spectrum, which can be deemed as spectral weights for fields under filtering, rises from 0 to 1, namely, the process slightly larger than the filter scale would be partially weakened, while the process much larger than the filter scale would be barely changed; When it is greater (smaller) than the characteristic wavenumber (spatial scale) of the filter, the spectral weight of boxcar filter oscillates up and down around the zero axis and converges rapidly, that is, the process of the smaller scale is nearly eliminated. In addition, the boxcar filter is equivalent to the mean value of all grid points in a given box (the weight is only determined by grid area or volume), which makes the flux on the box's boundary reflect the average change of the physical field inside the box, which is similar to latitude-longitude grid discretization and finite volume method. Therefore, we choose the boxcar filter for spatial coarse-graining.

From above, only when the scale of the selected explicit filter (the separation scale of spatial coarse-graining) is sufficiently larger than the scale of the implicit resolution filter the subfilter effect discussed be meaningful, and the data can be considered almost as DNS. Otherwise, it would lose too much local and non-local triad interaction for the subfilter scale, which might severely distort the microstructure of turbulence in the spectral space near the filter scale, making it impossible to reach a practical conclusion. Therefore, this paper focuses on the results under 2° boxcar filtering, which leaves a sufficient buffer zone between the implicit filter scales of SOSE and LICOM. This allows the local triad containing the subfilter scale wave vector that slightly smaller than the spatial separation scale to be reliable. Still, the influence of the non-local triad containing the smaller scale wave vector may be significantly underestimated.

Appendix B

Inspired by Kraichnan (1967); Gong et al. (1999); Vallis (2017); Zhou (2021), here we will discuss three categories of triad interaction in spectral space under scale separation of clear and unclear spectral truncation and reveal its relationship with Leonard's decomposition.

The free evolving PV equation in spectral space is,

$$\frac{\partial}{\partial t}\hat{q}(\mathbf{k}) = \sum_{\mathbf{k}=\mathbf{m}+\mathbf{n}} N(\mathbf{k} \mid \mathbf{m}, \mathbf{n}) \tag{B1}$$

$$q = \sum_{\mathbf{k}} \hat{q}(\mathbf{k}) e^{i\mathbf{k}\cdot\mathbf{x}} \tag{B2}$$

$$N(\mathbf{k} \mid \mathbf{m}, \mathbf{n}) = a_i(\mathbf{k})\hat{u}_i(\mathbf{m})\hat{q}(\mathbf{n}) \tag{B3}$$

N defines a single triad, i in Eq.B3 satisfies Einstein's summation convention, $\hat{u}_i$ is the velocity component in the spectral space, and a_i is weights related to the wavenumber caused by the partial-differential operator. Due to the orthogonality of the basis function, only the wave vectors $\mathbf{m}$ and $\mathbf{n}$, which can form a triangle with $\mathbf{k}$, would affect the evolution of the specified PV spectrum $\hat{q}(\mathbf{k})$. Given a clear truncation scale $\mathbf{k_c}$ in the spectral space, we can divide all wavenumbers in the whole spectral space into two cases: resolved (or filtered) and subgrid (or subfilter) wavenumbers, namely

$$\mathbf{k} = \begin{cases} \mathbf{k_r}, & if \ \ |\mathbf{k}| \leq \mathbf{k_c} \\ \mathbf{k_s}, & if \ \ |\mathbf{k}| > \mathbf{k_c} \end{cases} \tag{B4}$$

then the PV spectrum can be written as

$$\hat{q}(\mathbf{k}) = \begin{cases} \hat{q}_r\left(\mathbf{k_r}\right), & if \ \ |\mathbf{k}| \leq \mathbf{k_c} \\ \hat{q}_s\left(\mathbf{k_s}\right), & if \ \ |\mathbf{k}| > \mathbf{k_c} \end{cases} \tag{B5}$$

$$q_r = \sum_{\mathbf{k_r}} \hat{q}_r(\mathbf{k}) e^{i\mathbf{k}\cdot\mathbf{x}} \tag{B6}$$

$$q_s = \sum_{\mathbf{k_s}} \hat{q}_s(\mathbf{k}) e^{i\mathbf{k}\cdot\mathbf{x}} \tag{B7}$$

Apply Eq.B4 - Eq.B7 to Eq.B1, we obtain the resolved (or filtered) scale PV spectrum equation,

$$\frac{\partial}{\partial t}\hat{q}_r\left(\mathbf{k_r}\right) = N_r\left(\mathbf{k_r}\right) + N_{crs}\left(\mathbf{k_r}\right) + N_s\left(\mathbf{k_r}\right) \tag{B8}$$

$$N_r\left(\mathbf{k_r}\right) = \sum_{\mathbf{k_r}=\mathbf{m_r}+\mathbf{n_r}} N\left(\mathbf{k_r} \mid \mathbf{m_r}, \mathbf{n_r}\right) \tag{B9}$$

$$N_{crs}\left(\mathbf{k_r}\right) = \sum_{\mathbf{k_r}=\mathbf{m_r}+\mathbf{n_s}} N\left(\mathbf{k_r} \mid \mathbf{m_r}, \mathbf{n_s}\right) \ + \sum_{\mathbf{k_r}=\mathbf{m_s}+\mathbf{n_r}} N\left(\mathbf{k_r} \mid \mathbf{m_s}, \mathbf{n_r}\right) \tag{B10}$$

$$N_s\left(\mathbf{k_r}\right) = \sum_{\mathbf{k_r}=\mathbf{m_s}+\mathbf{n_s}} N\left(\mathbf{k_r} \mid \mathbf{m_s}, \mathbf{n_s}\right) \tag{B11}$$

The subscript $\mathbf{r}$ of this appendix means the quantity is in the resolved or filtered range, and the subscript $\mathbf{s}$ for subgrid or subfilter range. The right side of Eq.B8 includes three categories of triad terms with different microstructures: N_r represents the collective effect of two resolved wave vectors, namely $\mathbf{m_r}$ and $\mathbf{n_r}$, on the PV spectrum of a given wavenumber $\mathbf{k_r}$ at the resolved scale $\hat{q}_r\left(\mathbf{k_r}\right)$; N_{crs} represents the collective effect of two wave vectors from different ranges on $\hat{q}_r\left(\mathbf{k_r}\right)$; N_s represents the collective effect of two subgrid wave vectors $\mathbf{m_s}$ and $\mathbf{n_s}$.

Next, we consider the case that the scale separation is not clear spectral truncation, that is, the case of boxcar spatial coarse-graining adopted in this paper. According to the convolution theorem, the large spatial scale field $[q]$ and spatial eddying field q^* can be expressed as

$$[q] = q_r = \sum_{\mathbf{k}} \hat{G}(\mathbf{k})\hat{q}(\mathbf{k})e^{i\mathbf{k}\cdot\mathbf{x}} \tag{B12}$$

$$q^* = q_s = \sum_{\mathbf{k}} [1 - \hat{G}(\mathbf{k})]\hat{q}(\mathbf{k})e^{i\mathbf{k}\cdot\mathbf{x}} \tag{B13}$$

The separation scale now is not certain, so we generalize the separation scale into a separation scale interval,

$$\widetilde{\mathbf{k}_c} \in \left[\mathbf{k_c}^-, \mathbf{k_c}^+\right] \tag{B14}$$

$\mathbf{k_c}^-$ is the lower wavenumber bound with a significant magnitude of the subfilter quantity, and $\mathbf{k_c}^+$ is the upper wave number bound with a significant magnitude of the filtered field. The separation scale interval is the cross wave number interval of the two. In this way, the generalized resolved wave number $\widetilde{\mathbf{k}_r}$ and subgrid wave number $\widetilde{\mathbf{k}_s}$

$$\widetilde{\mathbf{k}_r} \in \left(0, \mathbf{k_c}^+\right] \tag{B15}$$

$$\widetilde{\mathbf{k}_s} \in \left[\mathbf{k_c}^-, \infty\right) \tag{B16}$$

generalize the spectrum of a specified quantity, for example for generalized PV spectrum

$$\hat{\widetilde{q}}(\mathbf{k}) \equiv \begin{cases} \hat{\widetilde{q}}_r\left(\widetilde{\mathbf{k_r}}\right) \equiv \hat{G}\left(\widetilde{\mathbf{k_r}}\right)\hat{q}\left(\widetilde{\mathbf{k_r}}\right), if\ \ \mathbf{k} \in filtered\ \ sector \\ \hat{\widetilde{q}}_s\left(\widetilde{\mathbf{k_s}}\right) \equiv \left[1 - \hat{G}\left(\widetilde{\mathbf{k_s}}\right)\right]\hat{q}\left(\widetilde{\mathbf{k_s}}\right), if\ \ \mathbf{k} \in subfiltered\ \ sector \end{cases} \tag{B17}$$

the generalized form of resolved (or filtered) scale PV spectrum equation is

$$\frac{\partial}{\partial t}\hat{\widetilde{q}}_r\left(\widetilde{\mathbf{k_r}}\right) = \widetilde{N_r}\left(\widetilde{\mathbf{k_r}}\right) + \widetilde{N_{crs}}\left(\widetilde{\mathbf{k_r}}\right) + \widetilde{N_s}\left(\widetilde{\mathbf{k_r}}\right) \tag{B18}$$

$$\widetilde{N_r}\left(\widetilde{\mathbf{k_r}}\right) = \sum_{\widetilde{\mathbf{k_r}}=\widetilde{\mathbf{m_r}}+\widetilde{\mathbf{n_r}}} \widetilde{N}\left(\widetilde{\mathbf{k_r}} \mid \widetilde{\mathbf{m_r}}, \widetilde{\mathbf{n_r}}\right) \tag{B19}$$

$$\widetilde{N_{crs}}\left(\widetilde{\mathbf{k_r}}\right) = \sum_{\widetilde{\mathbf{k_r}}=\widetilde{\mathbf{m_r}}+\widetilde{\mathbf{n_s}}} \widetilde{N}\left(\widetilde{\mathbf{k_r}} \mid \widetilde{\mathbf{m_r}}, \widetilde{\mathbf{n_s}}\right) + \sum_{\widetilde{\mathbf{k_r}}=\widetilde{\mathbf{m_s}}+\widetilde{\mathbf{n_r}}} \widetilde{N}\left(\widetilde{\mathbf{k_r}} \mid \widetilde{\mathbf{m_s}}, \widetilde{\mathbf{n_r}}\right) \tag{B20}$$

$$\widetilde{N_s}\left(\widetilde{\mathbf{k_r}}\right) = \sum_{\widetilde{\mathbf{k_r}}=\widetilde{\mathbf{m_s}}+\widetilde{\mathbf{n_s}}} \widetilde{N}\left(\widetilde{\mathbf{k_r}} \mid \widetilde{\mathbf{m_s}}, \widetilde{\mathbf{n_s}}\right) \tag{B21}$$

$$\widetilde{N}\left(\widetilde{\mathbf{k}} \mid \widetilde{\mathbf{m}}, \widetilde{\mathbf{n}}\right) = a_i\left(\widetilde{\mathbf{k}}\right)\hat{\widetilde{\mathbf{u}}}_{\mathbf{i}}\left(\widetilde{\mathbf{m}}\right)\hat{\widetilde{q}}\left(\widetilde{\mathbf{n}}\right) \tag{B22}$$

consistent with the form of Eq.B8 - Eq.B11 under clear spectrum truncation, there are three kinds of triad interaction terms with different microstructures. The difference is that their wave vectors have different number (0, 1, and 2) of subfilter quantities participating in the triad interaction. In Leonard's decomposition in this paper, $\widetilde{N_r}\left(\widetilde{\mathbf{k_r}}\right)$ corresponds to the sum of the Leonard term and large-scale transport term, $\widetilde{N_{crs}}\left(\widetilde{\mathbf{k_r}}\right)$ corresponds to the cross term, $\widetilde{N_s}\left(\widetilde{\mathbf{k_r}}\right)$ corresponds to the Reynolds term.

Appendix C

A brief example is given to illustrate the mass- or volume-weighted interpolation method: if the target neutral plane is $36.8kg/m^3$, for each water column, find the depths of neutral planes of 36.75 and $36.85kg/m^3$, and take the weighted average of the velocities on all z-coordinate levels between the two depths (the weight depends on the proportion of each z-coordinate level in the total depth difference, i.e., mass or volume weight) as the velocity on the 36.8kg/m3 neutral plane.

Another example illustrates how the least square regression of neighboring samples can solve the underdetermined problem when calculating the transport coefficient and tensor. For a given center point, say (120°E, 45°S), take the eddy flux and large-scale PV gradient on the neighboring $(2p+1)^2$ grid points as samples. Then least-square regress these $(2p+1)^2$ pairs of data to estimate quasi-localized transport tensor or coefficient at the central point (120°E, 45°S). This method has the advantages of convenience and a small amount of calculation and allows to handle the observed data or numerical results without enough numbers of passive tracers. In our method, the size of sampling area p would affect the reconstruction accuracy of the eddy flux. The smaller p is, the more localized the samples are, and the closer the reconstructed flux to the actual value. The smaller the ratio of sampling area size p to filter size ir, the smoother the physical field that makes the slowly varying hypothesis valid, and the higher the reconstruction accuracy. However, the influence of p/ir is not as dramatic as merely decreasing p. What we show in this paper is 9-point sampling with $p = 1$.

Acknowledgments

This study was supported by the National Natural Science Foundation of China (Grants 41931183, 41976026, and 41931182), the National Key RD Program for Developing Basic Sciences (2018YFA0605703), and the Strategic Priority Research Program of the Chinese Academy of Sciences (Grant No. XDB42010404). HLL and PFL also acknowledge the technical support from the National Key Scientific and Technological Infrastructure project "Earth System Science Numerical Simulator Facility" (EarthLab). Southern Ocean State Estimate (SOSE) data can be found in https://climatedataguide.ucar.edu/climate-data/southern-ocean-state-estimate-sose. The data and code used in the figures can be obtained online (http://data.lasg.ac.cn/lhl/data-hybrid-framework/).

References

Abernathey, R., & Cessi, P. (2014). Topographic enhancement of eddy efficiency in baroclinic equilibration. *Journal of Physical Oceanography*, *44*(8), 2107-2126. doi: 10.1175/JPO-D-14-0014.1

Aluie, H., Hecht, M., & Vallis, G. (2018). Mapping the energy cascade in the north atlantic ocean: The coarse-graining approach. *Journal of Physical Oceanography*, *48*(2), 225-244. doi: 10.1175/JPO-D-17-0100.1

Anderson, B., & Domaradzki, J. (2012). A subgrid-scale model for large-eddy simulation based on the physics of interscale energy transfer in turbulence. *Physics of Fluids*, *24*(6), 99-164. doi: 10.1063/1.4729618

Bachman, S. (2019). The gm+e closure: A framework for coupling backscatter with the gent and mcwilliams parameterization. *Ocean Modelling*, *136*, 85-106. doi: https://doi.org/10.1016/j.ocemod.2019.02.006

Bachman, S., & Fox-Kemper, B. (2013). Eddy parameterization challenge suite i: Eady spindown. *Ocean Modelling*, *64*(Complete), 12-28. doi: https://doi.org/10.1016/j.ocemod.2012.12.003

Bachman, S., Fox-Kemper, B., & Bryan, F. (2015). A tracer-based inversion method for diagnosing eddy-induced diffusivity and advection. *Ocean Modelling*, *86*, 1-14. doi: https://doi.org/10.1016/j.ocemod.2014.11.006

Bachman, S., Fox-Kemper, B., & Bryan, F. (2020). A diagnosis of anisotropic eddy diffusion from a high-resolution global ocean model. *Journal of Advances in Modeling Earth Systems*, *12*(2), e2019MS001904. doi: https://doi.org/10.1029/2019MS001904

Berloff, P. (2005). Random-forcing model of the mesoscale oceanic eddies. *Journal of Fluid Mechanics*, *529*, 71-95. doi: 10.1017/S0022112005003393

Bischoff, T., & Thompson, A. (2014). Configuration of a southern ocean storm track. *Journal of Physical Oceanography*, *44*(12), 3072-3078. doi: 10.1175/JPO-D-14-0062.1

Buzzicotti, M., Storer, B., Griffies, S., & Aluie, H. (2021). A coarse-grained decomposition of surface geostrophic kinetic energy in the global ocean. *Earth and Space Science Open Archive*, 58. doi: 10.1002/essoar.10507290.1

Cessi, P. (2007). An energy-constrained parameterization of eddy buoyancy flux. *Journal of Physical Oceanography*, *38*(8), 1807-1819. doi: 10.1175/2007JPO3812.1

Chapman, C., Hogg, A., Kiss, A., & Rintoul, S. (2015, 02). The dynamics of southern ocean storm tracks. *Journal of Physical Oceanography*, *45*, 150209131807009. doi: 10.1175/JPO-D-14-0075.1

Ciofalo, M. (1994). *Large-eddy simulation: A critical survey of models and applications*. Academic Press.

Clark, R. (1977). Evaluation of subgrid-scale turbulence models using a fully simulated turbulent flow.

Clark, R., Ferziger, J., & Reynolds, W. (1979). Evaluation of subgrid-scale models using an accurately simulated turbulent flow. *Jour Fluid Mech*, *91*(01), 1-16. doi: 10.1017/S002211207900001X

Dukowicz, J., & Smith, R. (1997). Stochastic theory of compressible turbulent fluid transport. *Physics of Fluids*, *9*(11), 3523-3529. doi: 10.1063/1.869460

Eden, C., & Greatbatch, R. (2008). Towards a mesoscale eddy closure. *Ocean Modelling*, *20*(3), 223-239. doi: 10.1016/j.ocemod.2007.09.002

Ferrari, R., & Nikurashin, M. (2010). Suppression of eddy diffusivity across jets in the southern ocean. *Journal of Physical Oceanography*, *40*(7), 1501-1519. doi: 10.1175/2010JPO4278.1

Fox-Kemper, B., Ferrari, R., & Pedlosky, J. (2003, 02). On the indeterminacy of rotational and divergent eddy fluxes. *Journal of Physical Oceanography - J PHYS OCEANOGR*, *33*, 478-483. doi: 10.1175/1520-0485(2003)033⟨0478:OTIORA⟩2.0.CO;2

Fox-Kemper, B., Lumpkin, R., & Bryan, F. (2013). *Lateral transport in the ocean interior*. International Geophysics. doi: https://doi.org/10.1016/B978-0-12-391851-2.00008-8

Fox-Kemper, B., & Menemenlis, D. (2008). Can large eddy simulation techniques improve mesoscale rich ocean models? *Washington DC American Geophysical Union Geophysical Monograph Series*, *177*, 319-337. doi: 10.1029/177GM19

Galmarini, S., Michelutti, F., & Thunis, P. (2000). Estimating the contribution of leonard and cross terms to the subfilter scale from atmospheric measurements. *J. Atmos. Sci.*. doi: 10.1175/1520-0469(2000)057⟨2968:etcola⟩2.0.co;2

Garabato, A., Ferrari, R., & Polzin, K. (2011). Eddy stirring in the southern ocean. *Journal of Geophysical Research*. doi: 10.1029/2010jc006818

Gent, & McWilliams, J. (1990). Isopycnal mixing in ocean circulation models. *Journal of Physical Oceanography*, *20*(1), 150-155. doi: 10.1175/1520-0485(1990)0202.0.CO;2

Gent, P., McDougall, T., & McWilliams, J. (1995). Parameterizing eddy-induced tracer transports in ocean circulation models. *J.phys.oceanogr*, *25*(4), 463-474. doi: 10.1175/1520-0485(1995)0252.0.CO;2

Germano, M. (1992). Turbulence-the filtering approach. *Journal of Fluid Mechanics*, *238*(-1). doi: 10.1017/S0022112092001733

Germano, M., Piomelli, U., Moin, P., & Cabot, W. (1991). A dynamic subgrid-scale eddy viscosity model. *Physics of Fluids*, *3*(3), 1760-1765. doi: https://doi.org/10.1063/1.857955

Gong, H., Chen, S., & He, G. (1999). An analysis of subgrid-resolved scale interactions with use of results from direct numerical simulations. *Acta Mechanica Sinica*. doi: 10.1007/BF02485875

Griffies, S. (1998). The gent–mcwilliams skew flux. *J.phys.oceanogr*, *28*(5), 831-841. doi: 10.1175/1520-0485(1998)0282.0.CO;2

Griffies, S., Gnanadesikan, A., Pacanowski, R., Larichev, V., & Smith, R. (1998). Isoneutral diffusion in a z-coordinate ocean model. *J.phys.oceanogr*, *28*(5), 805-830. doi: 10.1175/1520-0485(1998)0282.0.CO;2

Groeskamp, S., Lacasce, J., Mcdougall, T., & Rogé, M. (2020). Full-depth global estimates of ocean mesoscale eddy mixing from observations and theory. *Geophysical Research Letters*, *47*. doi: https://doi.org/10.1029/2020GL089425

Haigh, M., & Berloff, P. (2021). On co-existing diffusive and anti-diffusive tracer transport by oceanic mesoscale eddies. *Ocean Modelling*, *168*, 101909-. doi: https://doi.org/10.1016/j.ocemod.2021.101909

Haigh, M., Sun, L., Mcwilliams, J., & Berloff, P. (2021a). On eddy transport in the ocean. part ii: The advection tensor. *Ocean Modelling*, *165*. doi: 10.1016/j.ocemod.2021.101845

Haigh, M., Sun, L., Mcwilliams, J., & Berloff, P. (2021b). On eddy transport in the ocean. part i: The diffusion tensor. *Ocean Modelling*, *164*(1), 101831. doi: 10.1016/j.ocemod.2021.101831

Haigh, M., Sun, L., Shevchenko, I., & Berloff, P. (2020). Tracer-based estimates of eddy-induced diffusivities. *Deep Sea Research Part I Oceanographic Research Papers*, *160*, 103264. doi: https://doi.org/10.1016/j.dsr.2020.103264

Hallberg, R. (2013). Using a resolution function to regulate parameterizations of oceanic mesoscale eddy effects. *Ocean Modelling*, *72*(Complete), 92–103. doi: https://doi.org/10.1016/j.ocemod.2013.08.007

Hewitt, H., Roberts, M., Mathiot, P., Biastoch, A., & Zhang, Q. (2020). Resolving and parameterising the ocean mesoscale in earth system models. *Current Climate Change Reports*. doi: 10.1007/s40641-020-00164-w

Kamenkovich, I., Berloff, P., Haigh, M., Sun, L., & Lu, Y. (2021). Complexity of mesoscale eddy diffusivity in the ocean. *Geophysical Research Letters*, *48*(5), e2020GL091719. doi: https://doi.org/10.1029/2020GL091719

Khani, S., Jansen, M., & Adcroft, A. (2019). Diagnosing subgrid mesoscale eddy fluxes with and without topography. *Journal of Advances in Modeling Earth Systems*, *11*(12), 3995-4015. doi: https://doi.org/10.1029/2019MS001721

Kraichnan, R. H. (1967). Inertial ranges in two-dimensional turbulence. *Physics of Fluids*, *10*. doi: 10.1063/1.1762301

Ledwell, J., Watson, A., & Law, C. (1998). Mixing of a tracer in the pycnocline. *Journal of Geophysical Research Oceans*, *103*(C10), 21499-21529. doi: 10.1029/98JC01738

Leonard, A. (1974). Energy cascade in large-eddy simulations of turbulent fluid flows. In *Turbulent diffusion in environmental pollution.*

Liu, S., Meneveau, C., & Katz, J. (1994). On the properties of similarity subgrid-scale models as deduced from measurements in a turbulent jet. *J Fluid Mech*. doi: 10.1017/s0022112094002296

Lu, J., Wang, F., Liu, H., & Lin, P. (2016). Stationary mesoscale eddies, upgradient eddy fluxes, and the anisotropy of eddy diffusivity. *Geophysical Research Letters*, *43*(2), 743-751. doi: https://doi.org/10.1002/2015GL067384

MacCready, P., & Rhines, P. (2001). Meridional transport across a zonal channel: Topographic localization. *Journal of Physical Oceanography*, *31*(6), 1427-1439. doi: 10.1175/1520-0485(2001)0312.0.CO;2

Maddison, J., Marshall, D., & Shipton, J. (2015). On the dynamical influence of

ocean eddy potential vorticity fluxes. *Ocean Modelling*, *92*. doi: 10.1016/j.ocemod.2015.06.003

Mak, J., Marshall, D., Maddison, J., & Bachman, S. (2017). Emergent eddy saturation from an energy constrained eddy parameterisation. doi: https://doi.org/10.1016/j.ocemod.2017.02.007

Marshall, D., Maddison, J., & Berloff, P. (2012). A framework for parameterizing eddy potential vorticity fluxes. *Journal of Physical Oceanography*, *42*(4), 539-557. doi: 10.1175/JPO-D-11-048.1

Marshall, D., Williams, R., & Lee, M. (1999). The relation between eddy-induced transport and isopycnic gradients of potential vorticity. *J.phys.oceanogr*, *29*(7), 1571-1578. doi: doi:http://dx.doi.org/10.1175/1520-0485(1999)029⟨1571:TRBEIT⟩2.0

Mazloff, M., Heimbach, P., & Wunsch, C. (2010). An eddy-permitting southern ocean state estimate. *Journal of Physical Oceanography*, *40*(5), 880-899. doi: 10.1175/2009JPO4236.1

McDougall, T. (1987). Neutral surfaces. *Journal of Physical Oceanography*, *17*(17), 1950-1964. doi: 10.1175/1520-0485(1987)017⟨1546:CISSA⟩2.0.CO;2

McDougall, T., & McIntosh, P. (1996). The temporal-residual-mean velocity. part i: Derivation and the scalar conservation equations. *Journal of Physical Oceanography*, *26*(12), 2653-2665. doi: 10.1175/1520-0485(1996)0262.0.CO;2

Mcdougall, T., & Mcintosh, P. (2001). The temporal-residual-mean velocity. part ii: Isopycnal interpretation and the tracer and momentum equations. *Journal of Physical Oceanography*, *31*(5), 1222-1246. doi: 10.1175/1520-0485(2001)0312.0.CO;2

Nakamura, N. (2001). A new look at eddy diffusivity as a mixing diagnostic. *Journal of the Atmospheric Sciences*, *58*(24), 3685-3701. doi: 10.1175/1520-0469(2001)058⟨3685:anlaed⟩2.0.co;2

Radko, T., & Kamenkovich, I. (2017). On the topographic modulation of large-scale eddying flows. *Journal of Physical Oceanography*, *47*(9), 2157-2172. doi: 10.1175/JPO-D-17-0024.1

Redi, M. (1982). Oceanic isopycnal mixing by coordinate rotation. *Journal of Physical Oceanography*, *12*(10), 1154-1158. doi: 10.1175/1520-0485(1982)0122.0.CO;2

Rintoul, S. R., Hughes, C. W., & Olbers, D. J. (2001). The antarctic circumpolar current system. *Ocean Circulation Climate*(01), 271–302, XXIX–XXXVI. doi: 10.1016/S0074-6142(01)80124-8

Rypina, I., Kamenkovich, I., Berloff, P., & Pratt, L. J. (2012). Eddy-induced particle dispersion in the near-surface north atlantic. *Chaos An Interdisciplinary Journal of Nonlinear Science*, *42*(12), 2206-2228. doi: 10.1063/1.4927424

Smith, R., & Gent, P. (2004). Anisotropic gent–mcwilliams parameterization for ocean models. *Journal of Physical Oceanography*, *34*(11), 2541. doi: 10.1175/JPO2613.1

Smith, S. (2005). Tracer transport along and across coherent jets in two-dimensional turbulent flow. *Journal of Fluid Mechanics*, *544*(-1), 133-142. doi: 10.1017/S0022112005006750

Speziale, C. (1985). Galilean invariance of subgrid-scale stress models in the large-eddy simulation of turbulence. *Journal of Fluid Mechanics*, *156*(156), 55-62. doi: 10.1017/S0022112085001987

Srinivasan, K., & Young, W. (2014). Reynolds stress and eddy diffusivity of -plane shear flows. *Journal of the Atmospheric Sciences*, *71*(6), 2169 - 2185. doi: 10.1175/JAS-D-13-0246.1

Stanley. (2019). Neutral surface topology. *Ocean Modelling*. doi: 10.1016/j.ocemod.2019.01.008

Stanley, Z., Bachman, S., & Grooms, I. (2020). Vertical structure of ocean mesoscale eddies with implications for parameterizations of tracer transport. *Journal*

of Advances in Modeling Earth Systems, *12*. doi: https://doi.org/10.1029/2020MS002151

Sun, L., Haigh, M., Shevchenko, I., Berloff, P., & Kamenkovich, I. (2021, 08). On non-uniqueness of the mesoscale eddy diffusivity. *Journal of Fluid Mechanics*, *920*. doi: 10.1017/jfm.2021.472

Taylor, G. (1922). Diffusion by continuous movements. *Proceedings of the London Mathematical Society*, *s2-20*(1). doi: 10.1112/plms/s2-20.1.196

Thompson, A., & Garabato, A. (2014). Equilibration of the antarctic circumpolar current by standing meanders. *Journal of Physical Oceanography*, *44*(7), 1811 - 1828. doi: 10.1175/JPO-D-13-0163.1

Thompson, A., & Sallée, J. (2012). Jets and topography: Jet transitions and the impact on transport in the antarctic circumpolar current. *Journal of Physical Oceanography*, *42*(6), 956-972. doi: 10.1175/JPO-D-11-0135.1

Thompson, A. F. (2010). Jet formation and evolution in baroclinic turbulence with simple topography. *J.phys.oceanogr*, *40*(2), 257–278. doi: http://dx.doi.org/10.1175/2009JPO4218.1

Treguier, A., Held, I., & Larichev, V. (1997). Parameterization of quasigeostrophic eddies in primitive equation ocean models. *J.phys.oceanogr*, *27*(4), 567-580. doi: 10.1175/1520-0485(1997)0272.0.CO;2

Treguier, A., & McWilliams, J. (1990). Topographic influences on wind-driven, stratified flow in a -plane channel: An idealized model of the antarctic circumpolar current. *J. Phys. Ocean.*, *20*, 324-343. doi: 10.1175/1520-0485(1990)020⟨0321:TIOWDS⟩2.0.CO;2

Vallis, G. (2017). *Atmospheric and oceanic fluid dynamics*.

Visbeck, M., Marshall, J., Haine, T., & Spall, M. (1997). Specification of eddy transfer coefficients in coarse-resolution ocean circulation models. *Journal of Physical Oceanography*, *27*(3), 381-402. doi: 10.1175/1520-0485(1997)0272.0.CO;2

Waterman, S., & Lilly, J. M. (2015, April). Geometric Decomposition of Eddy Feedbacks in Barotropic Systems. *Journal of Physical Oceanography*, *45*(4), 1009-1024. doi: 10.1175/JPO-D-14-0177.1

Wei, H., & Wang, Y. (2021). Full-depth scalings for isopycnal eddy mixing across continental slopes under upwelling-favorable winds. *Journal of Advances in Modeling Earth Systems*, *13*. doi: 10.1029/2021MS002498

Williams, Richard, G., Wilson, Chris, Hughes, ... W. (2007). Ocean and atmosphere storm tracks: The role of eddy vorticity forcing. *J. Phys. Oceanogr*. doi: 10.1175/jpo3120.1

Young, W., Rhines, P., & Garrett, C. (1982). Shear-flow dispersion, internal waves and horizontal mixing in the ocean. *Journal of Physical Oceanography*, *12*(6), 515–527.

Youngs, M., Thompson, A., Lazar, A., & Richards, K. (2017). Acc meanders, energy transfer, and mixed barotropic-baroclinic instability. *Journal of Physical Oceanography*, *47*(6), 1291-1305. doi: 10.1175/JPO-D-16-0160.1

Yu, Y. Q., Liu, H. L., & Lin, P. F. (2012). A quasi-global 1/10° eddy-resolving ocean general circulation model and its preliminary results. *Chinese Science Bulletin*. doi: 10.1007/s11434-012-5234-8

Zhai, X., Johnson, H., & Marshall, D. (2010, 08). Significant sink of ocean-eddy energy near western boundaries. *Nature Geoscience*, *3*. doi: 10.1038/ngeo943

Zhou, Y. (2021). Turbulence theories and statistical closure approaches. *Physics Reports*, *935*(Suppl. 1). doi: 10.1016/j.physrep.2021.07.001

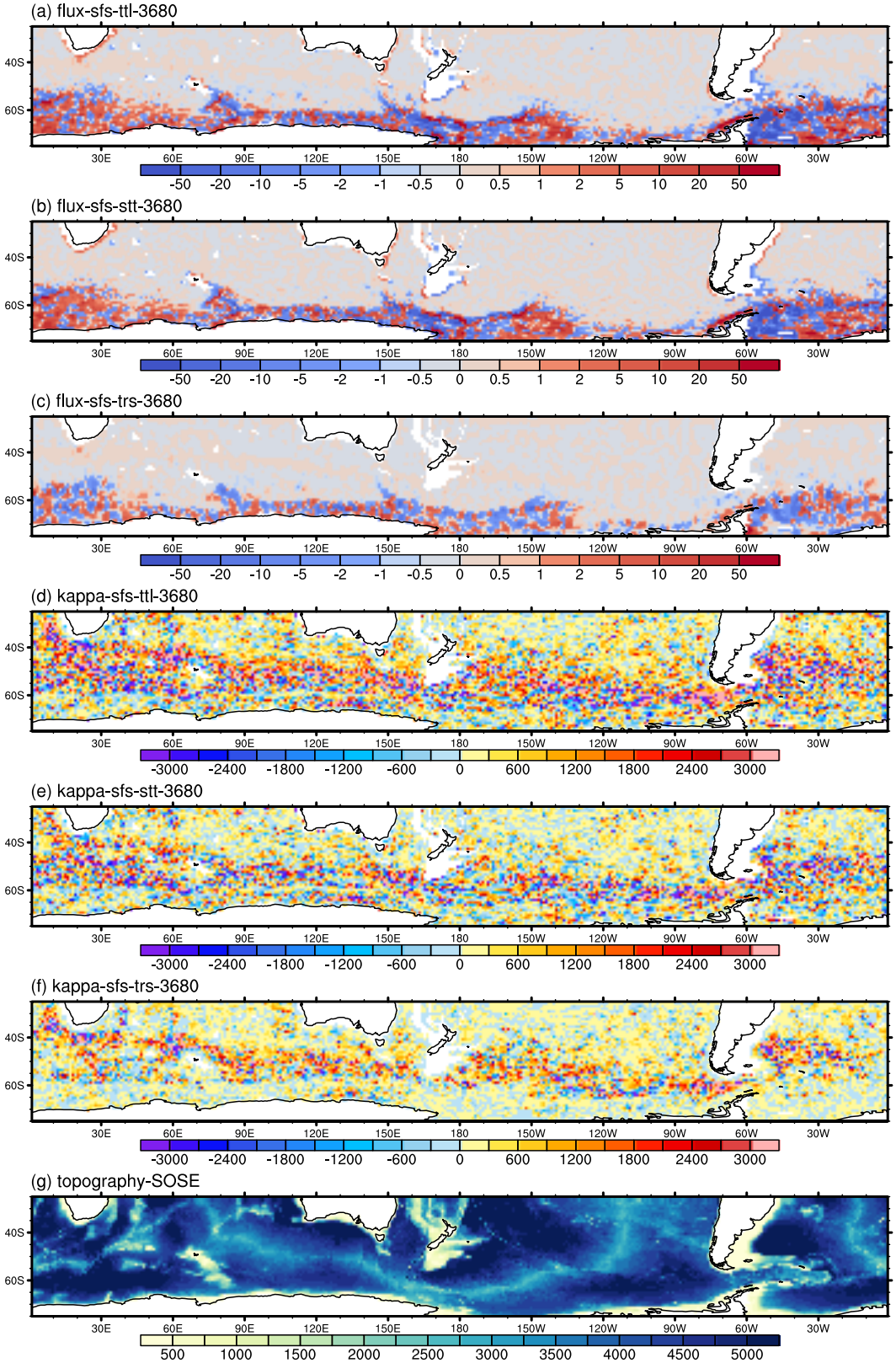

Figure C1. (a) total, (b) stationary, and (c) transient meridional subfilter PV flux, unit: $10^{-13}s^{-2}$, (d) total, (e) stationary, and (f) transient isotropic subfilter transport coefficient, unit m^2/s, on the topobaric surface of $36.8kg/m^3$, using 2° boxcar filter for SOSE, (g) large-scale topography (filtered by 2° boxcar filter) of SOSE, unit: m

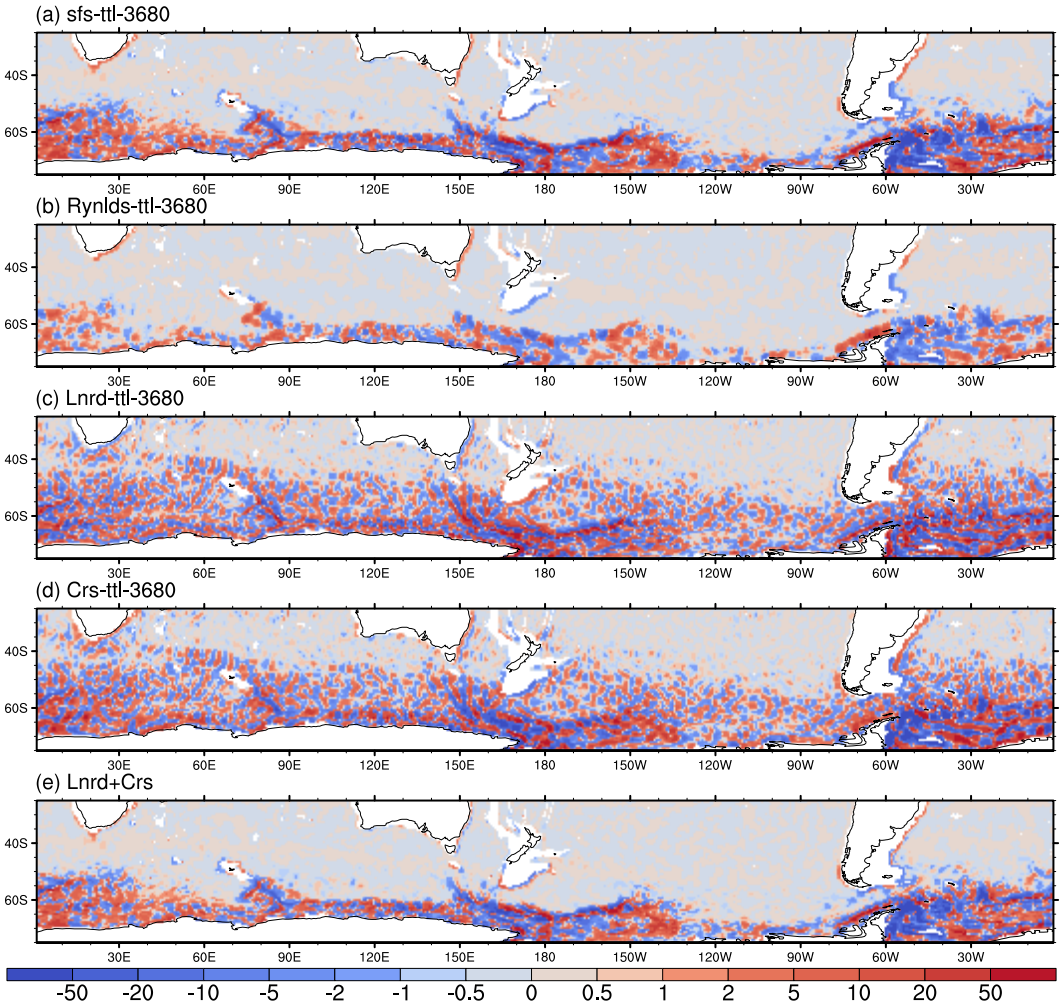

Figure C2. The total meridional subfilter PV flux of (a) complete subfilter, (b) Reynolds term, (c) Leonard term, (d) Cross term and (e) Leonard plus Cross term, unit: 1e-13 S-2, on the topobaric surface of $36.8 kg/m^3$, using 2° boxcar filter for SOSE

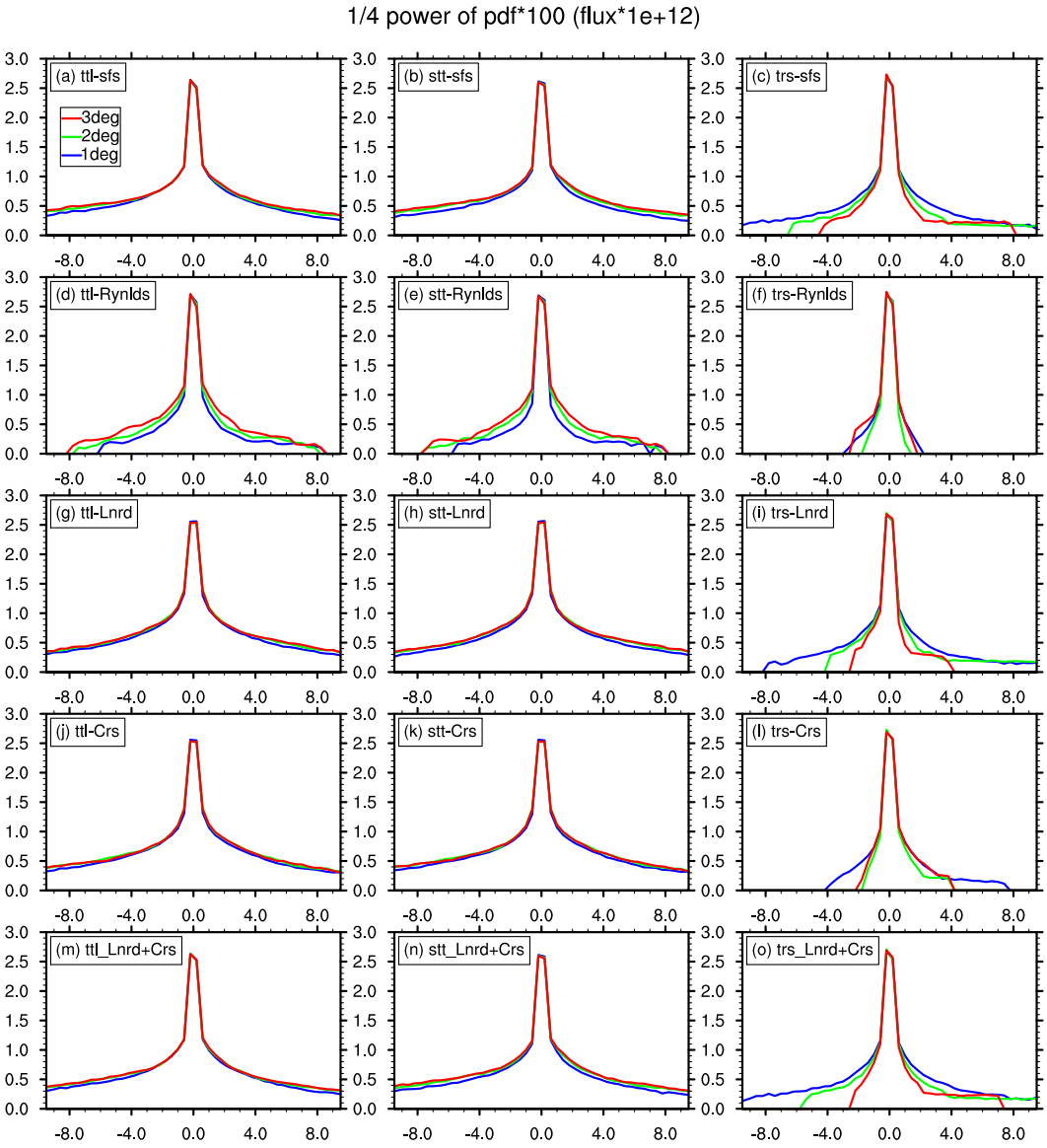

Figure C3. 1/4 power of the PDF of the meridional subfilter PV flux ($10^{-12}s^{-2}$) of SOSE, this scaling is for the convenience of drawing. The three columns from left to right are the total, stationary and transient parts, respectively. The five rows from top to bottom are the results of subfilter, Reynolds term, Leonard term, Cross term and the sum of Leonard and Cross term, respectively. blue, green ,and red line for 1°, 2°, and 3° boxcar filter, respectively.

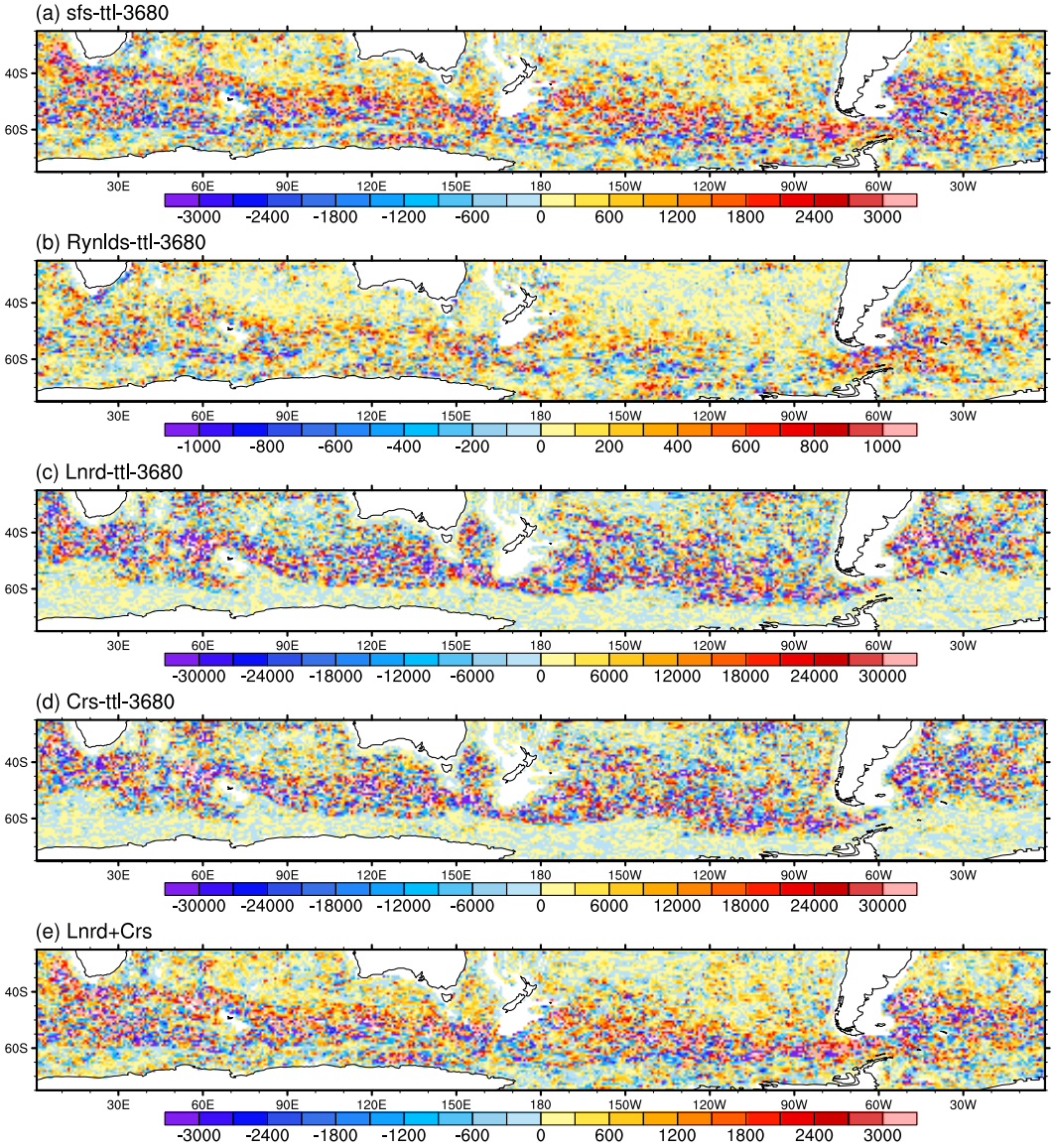

Figure C4. The eddy transport coefficient of (a) complete subfilter, (b) Reynolds term, (c) Leonard term, (d) Cross term and (e) Leonard plus Cross term, unit: m^2/s, on the topobaric surface of $36.8kg/m^3$, using 2° boxcar filter for SOSE

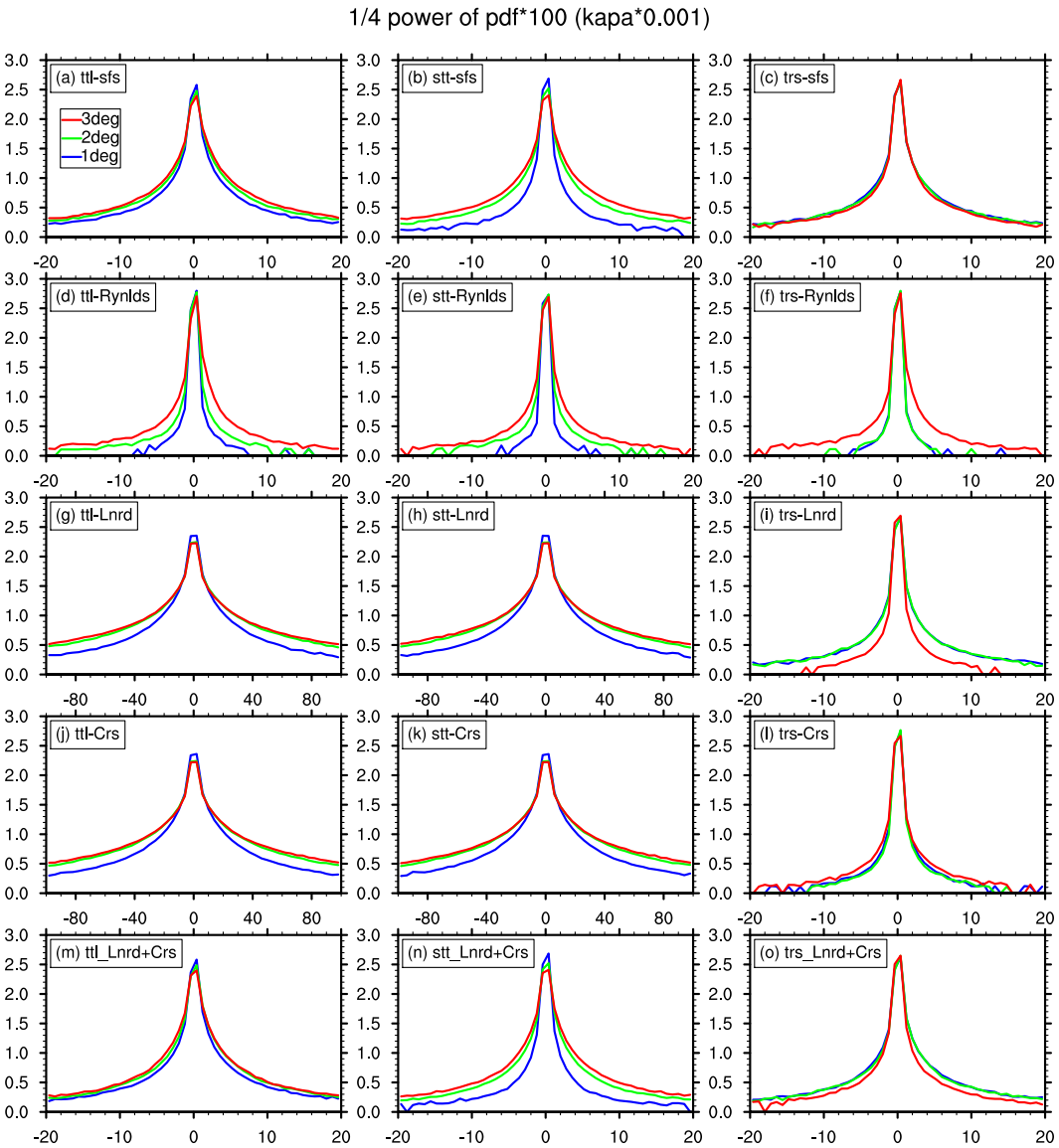

Figure C5. The same as Figure 3, but for the eddy transport coefficient $10^3 m^2/s$

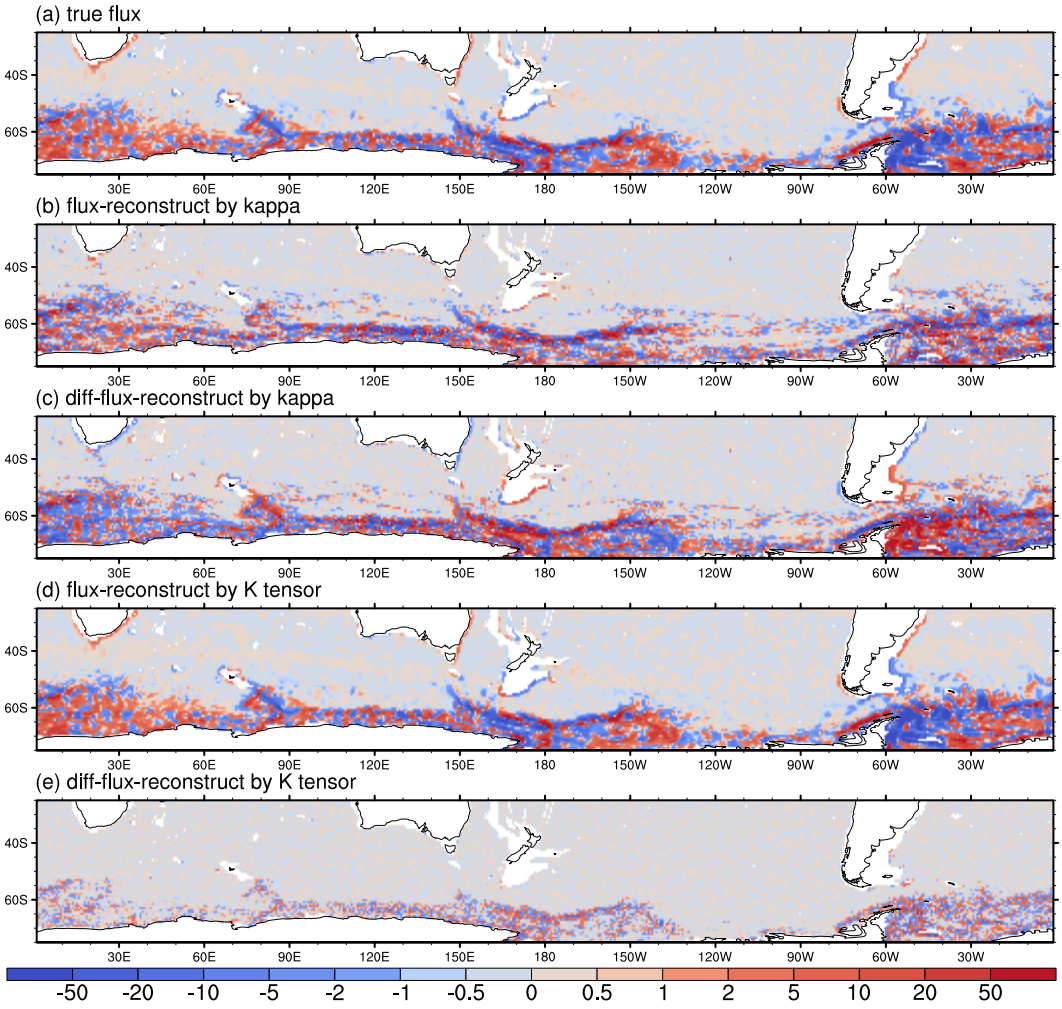

Figure C6. (a) The total meridional subfilter PV flux, (b) the flux reconstructed by the isotropic transport coefficient, (c) the difference between the isotropic reconstruction and true flux, (d) the flux reconstructed by the anisotropic transport tensor, and (e) the difference between the anisotropic reconstruction and true flux, on the topobaric surface of $36.8 kg/m^3$, using 2° boxcar filter for SOSE

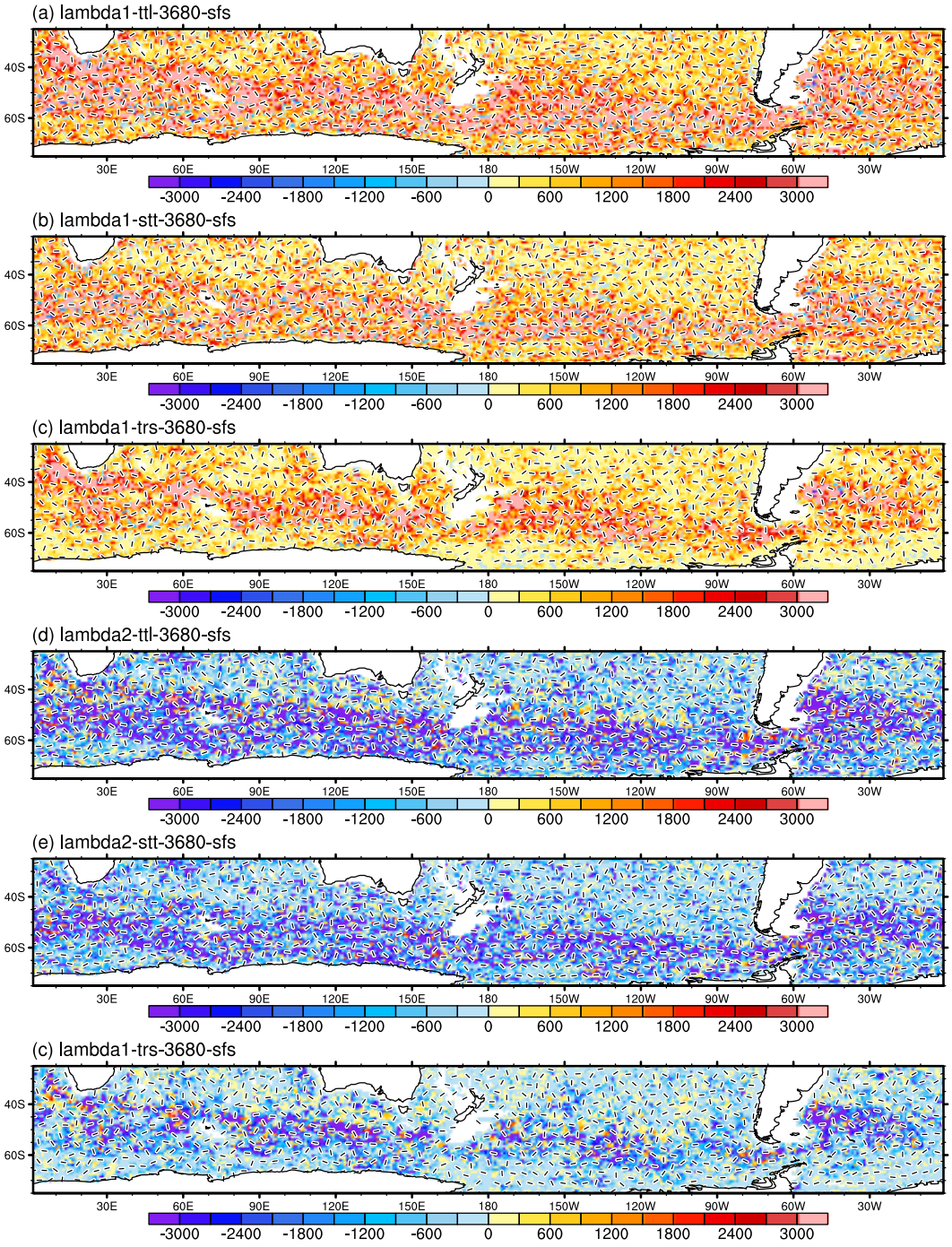

Figure C7. (a) (b) (c) is the total, stationary, and transient major transport eigenvalue respectively, (d) (e) (f) for the minor eigenvalue, on the topobaric surface of $36.8 kg/m^3$, using 2° boxcar filter for SOSE

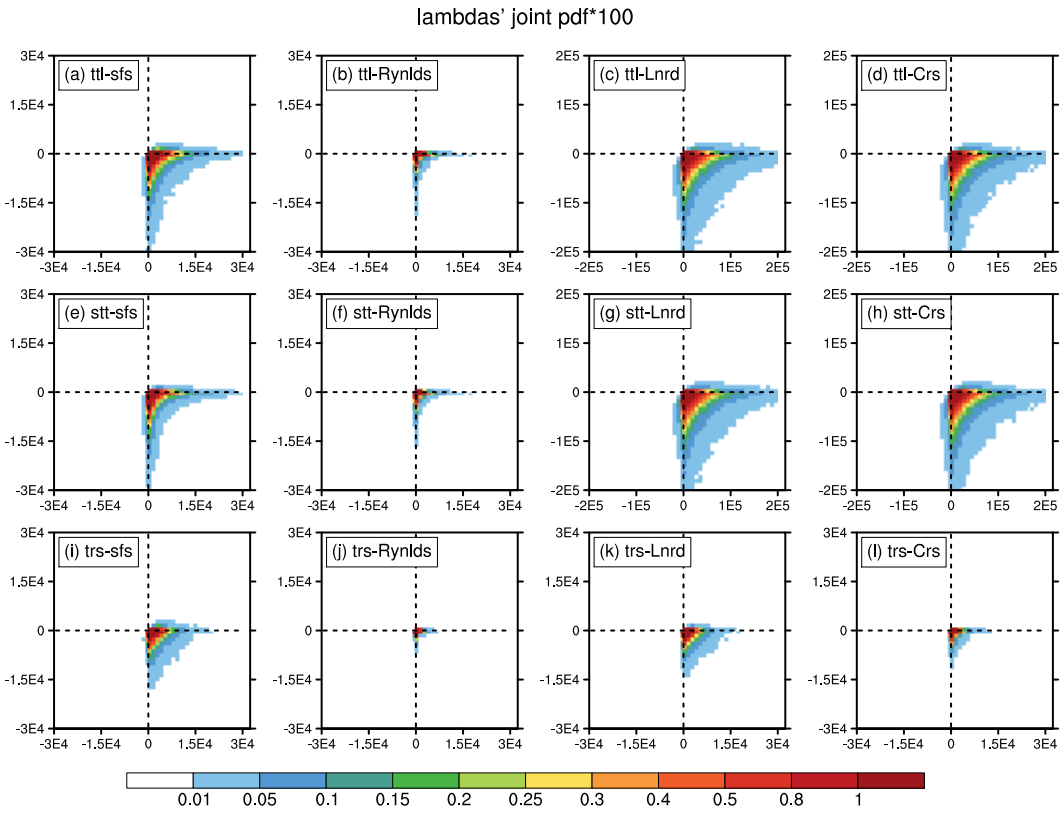

Figure C8. The joint PDF of the two eigenvalues of SOSE under 2° boxcar filter. The three rows from top to bottom are the total, stationary, and transient, respectively. The four columns from left to right are the results of complete subfilter, Reynolds term, Leonard term, and Cross term, respectively. The x- and y-coordinate represent the variation range of the major and minor eigenvalue, respectively (note that the coordinate range of different terms might be different). Values that are beyond the coordinate range or less than 10^{-4} are not shown. The bin interval is 1/25 of the maximum coordinate value.

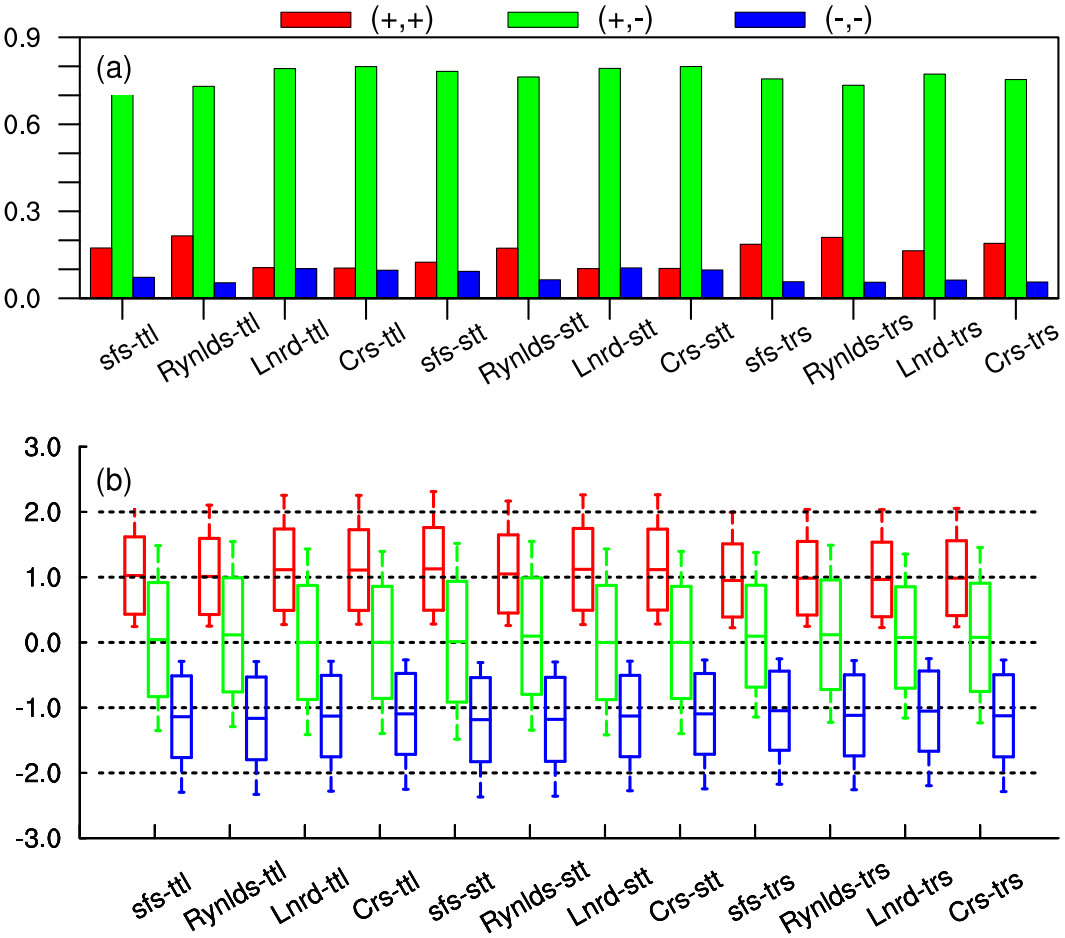

Figure C9. (a) The frequency of three eigenvalue combinations, (b) the degree of anisotropy, that is, the log_{10} of the absolute value of the ratio of the major eigenvalue to the minor eigenvalue, on the topobaric surface of $36.8 kg/m^3$, using 2° boxcar filter for SOSE. Red is (major+, minor+), green is (major+, minor-), and blue is (major-, minor-).

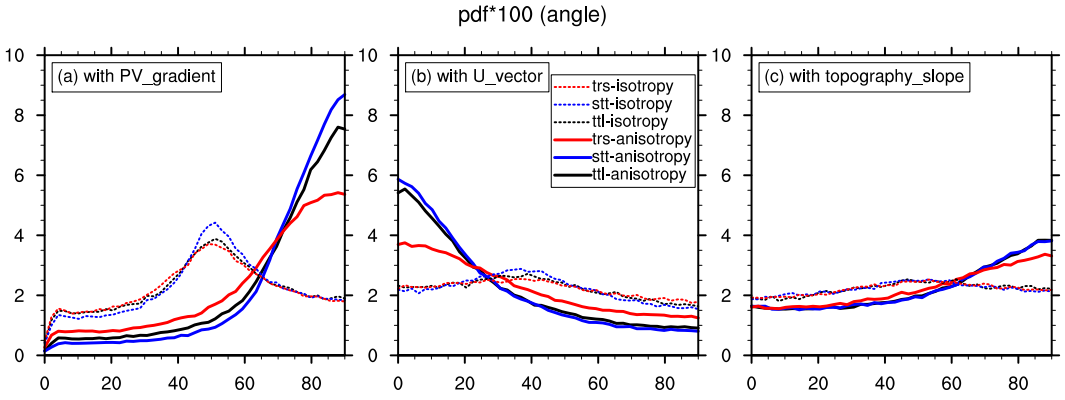

Figure C10. The PDF of the angle between the dominant eigenvector and the (a) topographic slope, (b) PV grandient and (c) velocity vector, on the topobaric surface of $36.8 kg/m^3$, using 2° boxcar filter for SOSE. The solid line is for strong anisotropic region where $|\lambda_1/\lambda_2| > 5$ or $|\lambda_1/\lambda_2| < 1/5$, and the dotted line is for weak anisotropic region where $|\lambda_1/\lambda_2| < 1/2$ and $|\lambda_1/\lambda_2| > 1/2$. Black, blue, and red lines are for total, stationary, and transient parts, respectively. The topographic slope, PV grandient and velocity vector have also been 2° boxcar filtered

S1

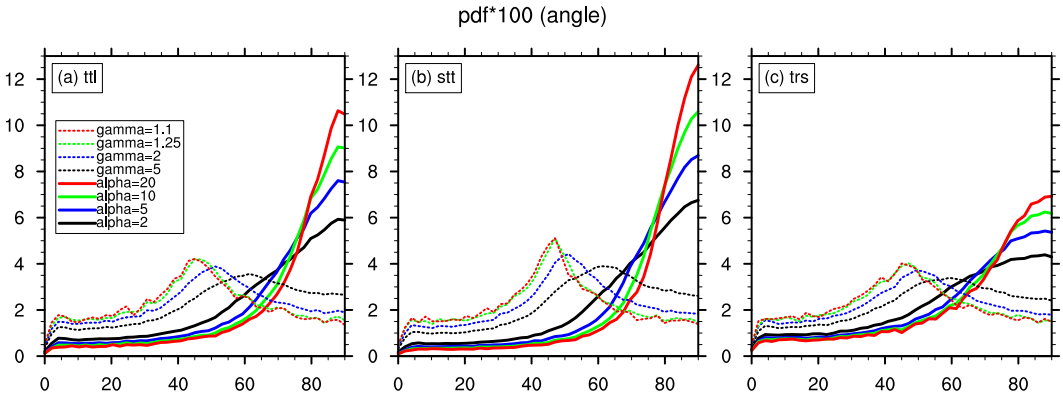

Figure C11. The PDF of the angle between the (a) total, (b) stationary, and (c) transient dominant eigenvector and the large-scale PV grandient on the topobaric surface of $36.8kg/m^3$, using 2° boxcar filter for SOSE. The solid line is for strong anisotropic region with $\alpha = 2, 5, 10, 20$, and the dotted line is for weak anisotropic region with $\gamma = 1.1, 1.25, 2, 5$.